

# JGR Atmospheres

## RESEARCH ARTICLE

10.1029/2021JD034704

### Key Points:

- Electrification of winter clouds occurs in the absence of lightning, and mixed phase microphysics is observed near enhanced electric fields
- Observed electric fields were as high as  $80 \text{ V m}^{-1}$  and variability in the electric field was observed along the flight path of the ER-2
- Electrification within winter clouds can be identified using depolarization streaks in differential reflectivity

### Correspondence to:

C. J. Schultz,  
[christopher.j.schultz@nasa.gov](mailto:christopher.j.schultz@nasa.gov)

### Citation:

Schultz, C. J., Harkema, S. S., Mach, D. M., Bateman, M., Lang, T. J., Heymsfield, G. M., et al. (2021). Remote sensing of electric fields observed within winter precipitation during the 2020 Investigation of Microphysics and Precipitation for Atlantic Coast-Threatening Snowstorms (IMPACTS) field campaign. *Journal of Geophysical Research: Atmospheres*, 126, e2021JD034704. <https://doi.org/10.1029/2021JD034704>

Received 3 FEB 2021

Accepted 2 AUG 2021

### Author Contributions:

**Conceptualization:** Christopher J. Schultz, Sebastian S. Harkema, Douglas M. Mach

**Data curation:** Christopher J. Schultz, Sebastian S. Harkema, Douglas M. Mach, Monte Bateman, Matthew L. McLinden, Lihua Li

**Formal analysis:** Christopher J. Schultz, Sebastian S. Harkema, Douglas M. Mach, Monte Bateman, Michael Poellot, Kendra Sand

**Funding acquisition:** Christopher J. Schultz, Timothy J. Lang, Gerald M. Heymsfield

**Investigation:** Christopher J. Schultz, Sebastian S. Harkema, Douglas M.

## Remote Sensing of Electric Fields Observed Within Winter Precipitation During the 2020 Investigation of Microphysics and Precipitation for Atlantic Coast-Threatening Snowstorms (IMPACTS) Field Campaign

Christopher J. Schultz<sup>1</sup> , Sebastian S. Harkema<sup>2</sup>, Douglas M. Mach<sup>3</sup> , Monte Bateman<sup>2</sup> , Timothy J. Lang<sup>1</sup> , Gerald M. Heymsfield<sup>4</sup> , Matthew L. McLinden<sup>4</sup>, Lihua Li<sup>4</sup>, Michael Poellot<sup>5</sup>, and Kendra Sand<sup>5</sup>

<sup>1</sup>Earth Science Branch, NASA Marshall Space Flight Center, Huntsville, AL, USA, <sup>2</sup>Department of Atmospheric Science, University of Alabama Huntsville, Huntsville, AL, USA, <sup>3</sup>Science and Technology Institute, Universities Space Research Association, Huntsville, AL, USA, <sup>4</sup>Goddard Space Flight Center, Greenbelt, MD, USA, <sup>5</sup>Department of Atmospheric Science, University of North Dakota, Grand Forks, ND, USA

**Abstract** Aircraft electric fields from NASA's Lightning Instrument Package (LIP) were coupled with other airborne and ground-based, and in situ measurements to understand electrification in winter clouds that did not produce lightning. The measurements were made during seven research flights by a NASA ER-2 during the 2020 Investigation of Microphysics and Precipitation for Atlantic Coast-Threatening Snowstorms (IMPACTS) campaign. Observed total electric field magnitudes were as high as  $80 \text{ V m}^{-1}$  and variability in the electric field was observed along the flight path of the ER-2, indicating horizontal and/or vertical inhomogeneity in the cloud's electrical structure. X-band airborne radar data indicated 20-dBZ echo tops above 5 km in regions where electrification exceeded  $10 \text{ V m}^{-1}$ . In these regions, 85-GHz brightness temperatures ( $T_B$ ) from an airborne radiometer were lower than 265 K, with the lowest  $T_B$  ( $\sim 210 \text{ K}$ ) associated with ice scattering collocated with the strongest electric fields. In situ microphysical measurements from the NASA P-3 aircraft on February 7 indicated that regions near strong electric field contained supercooled water, rimed ice hydrometeors, ice water p- content as high as  $1 \text{ g m}^{-3}$ , liquid water content as high as  $0.15 \text{ g m}^{-3}$ , and supersaturation as high as 3.5%. These observations support the role of mixed phase microphysics in the generation of electric fields in clouds. In three case studies, ground based S-band polarimetric radar observed depolarization streaks in differential reflectivity near areas where the strongest electrification was observed. This observation reinforces the utility of depolarization streaks to identify areas of electrification prior to lightning occurrence.

**Plain Language Summary** Electrification of winter clouds is not well characterized unless lightning is observed. The goal of this work is to understand how winter clouds electrify and the microphysical characteristics that support electrification for non-lightning producing clouds. Using a unique system of aircraft-based electric field mills, the electric field of winter clouds was measured and compared against radar and in cloud observations of liquid water, ice, temperature, and relative humidity to determine the conditions in which electrification are observed. Results indicate that when ice orientation is observed in radar data, strong electric fields are also within the same volume of the cloud. The impact of this study is that radar data can be used to determine locations where lightning may be possible prior to observed lightning.

## 1. Introduction

Lightning is commonly used to indicate the presence of heavy snowfall potential in winter cyclones because there is a common microphysical environment that enhances both dendritic growth of ice crystals (IC) and cloud electrification (e.g., Adhikari & Liu, 2019; Crowe et al., 2006; Harkema et al., 2019; Kumjian & Deierling, 2015; Market et al., 2006; Market & Becker, 2009; Schultz et al., 2018; Rauber et al., 2014). Recent work by Harkema et al. (2020) found that the largest snowfall rates and snow-to-liquid ratios were displaced from lightning occurrence, while total snowfall were spatially well-correlated during the first year of operationally viable GLM observations in 2018. They postulated that the reason for the displacement between the

Mach, Monte Bateman, Gerald M. Heymsfield, Michael Poellot  
**Methodology:** Christopher J. Schultz, Sebastian S. Harkema, Douglas M. Mach, Michael Poellot, Kendra Sand  
**Project Administration:** Christopher J. Schultz, Timothy J. Lang  
**Resources:** Christopher J. Schultz, Timothy J. Lang, Gerald M. Heymsfield  
**Software:** Christopher J. Schultz, Sebastian S. Harkema, Douglas M. Mach, Monte Bateman, Matthew L. McLinden, Lihua Li  
**Supervision:** Christopher J. Schultz, Timothy J. Lang  
**Validation:** Christopher J. Schultz, Sebastian S. Harkema, Douglas M. Mach  
**Visualization:** Christopher J. Schultz, Sebastian S. Harkema, Douglas M. Mach, Matthew L. McLinden, Lihua Li  
**Writing – original draft:** Christopher J. Schultz, Sebastian S. Harkema, Douglas M. Mach  
**Writing – review & editing:** Christopher J. Schultz, Sebastian S. Harkema, Douglas M. Mach, Monte Bateman, Timothy J. Lang, Gerald M. Heymsfield, Matthew L. McLinden, Michael Poellot, Kendra Sand

observed lightning location and heaviest snowfall totals is because the mechanisms that drive electrification and dendritic growth in winter cyclones aloft take time to reach the surface, and thus can undergo horizontal advection due to low fall speeds that are around 1–1.5 m s<sup>-1</sup> or less (Heymsfield & Kajikawa, 1987; Heymsfield & Westbrook, 2010; Locatelli & Hobbs, 1974; Molthan & Petersen, 2011). However, other than the physical occurrence of lightning, very little is known about electric fields generated in snow-bearing clouds, especially clouds that do not generate lightning.

The most comprehensive electric field measurements in winter cyclones were obtained from winter storms in the Sea of Japan (e.g., Brook et al., 1982; Kitagawa & Michimoto, 1994; Takeuti et al., 1978), where they examined lightning flashes in winter storms that produced positive cloud-to-ground flashes (+CG). Brook et al. (1982) inferred that wind shear was responsible for the generation of +CG flashes as the electric field measurements indicated that charge structures in these winter storms consisted of a main positive charge region over but offset from a main negative charge region. A main positive over the main negative charge structure was also observed by Rust and Trapp (2002) using balloon-borne soundings in winter nimbostratus in Utah. Since the publication of these studies, very little has been published regarding background electric field measurements during snowfall events except for research that focused on the electrical characteristics of blowing snow at the surface (e.g., Gordon & Taylor, 2009; Yair et al., 2019).

Brook et al. (1982) and Kitagawa and Michimoto (1994) provided schematics related to charge structure and variability within winter storms near the Sea of Japan. Using ground-based electric field mills, they found that there were different charge structures that were fundamentally tied to the maturity of the parent cloud. Rust and Trapp (2002) highlighted vertical variability in the electric field in winter nimbostratus in Utah, where two to four different charge layers were present above the melting layer. Schultz et al. (2018) inferred charge structure within the cloud using lightning mapping array (LMA) measurements and found that winter systems in Alabama, Oklahoma, and near Washington, D.C. primarily featured a positive charge layer above a negative charge layer. However, they observed one flash where positive and negative polarity ground flashes occurred out of the same area of enhanced snowfall, and the LMA indicated the potential for heterogeneous charge structures within the parent cloud.

With the lack of direct electric field measurements and the increase in polarimetric radars worldwide, researchers and forecasters use polarimetric variables like differential reflectivity ( $Z_{DR}$ ; Seliga & Bringi, 1976) to identify depolarization streaks in radar radials (e.g., Hendry & McCormick, 1976; Krehbiel et al., 1996; Ryzhkov, 2007; Hubbert et al., 2014) and thus active electrification in the cloud. Radars like those in the United States National Weather Service polarimetric radar network are ideal for depolarization streak detection in  $Z_{DR}$  because these radars operate in simultaneous transmit and receive mode (STAR; Doviak et al., 2000; Ryzhkov & Zrnić, 2007; Scott et al., 2001). When polarimetric radars are in STAR mode, cross coupling of the horizontal and vertical returned wave components occurs after the transmitted wave encounters IC aligned in a vertical electric field, and the depolarization streak in  $Z_{DR}$  indicates that the mean canting angle of the IC is not horizontal (Hubbert et al., 2010, 2014; Ryzhkov & Zrnić, 2007; Wang & Chandrasekar, 2006). When the minor axis of the hydrometeor is not perfectly aligned in the vertical due to effects from the electric field of the cloud; scattering of both the horizontal and vertical polarization radar signal is possible, resulting in the appearance of streaks in the  $Z_{DR}$  fields (Kumjian, 2013). Depolarization streaks in  $Z_{DR}$  are most prominent in regions where there is a large precipitation shield, such as winter storms and large stratiform and anvil regions associated with thunderstorms (e.g., Kumjian & Deierling, 2015; Schultz et al., 2021), where updraft structures are broad, resulting in slower charge separation and stronger electric fields (e.g., Bateman et al., 1995; Rust & Trapp, 2002; Schuur & Rutledge, 2000). Electric field measurements associated with depolarization streaks do not exist in the literature for winter storms; therefore, a gap in knowledge exists between the magnitude of the electric field and the depth at which depolarization is observed in the radar data.

The 2020 Investigation of Microphysics and Precipitation for Atlantic Coast-Threatening Snowstorms (IMPACTS; McMurdie et al., 2019, 2020) field program provides the opportunity to address some of these gaps in knowledge for winter storms using aircraft, ground-based, and in situ observations. The goals of the present study are to:

1. Characterize total electric field magnitudes in non-lightning producing winter precipitation structures observed during the 2020 IMPACTS field campaign.



**Figure 1.** Images of the Lightning Instrument Package field mills, data box (panel A), and locations on the ER-2 Aircraft (panels B, C). Not shown are the three mills on the left wing, two of them mirroring the location on the right wing, and a third on the lower aft part of the left superpod.

2. Use precipitation characteristics observed by radar, passive microwave instrumentation, and in situ probe information to diagnose the microphysical structure relative to total electric field magnitude.
3. Characterize total electric field magnitudes observed in the presence of depolarization streaks in  $Z_{DR}$  to determine the total electric field variability in the presence of these radar based indicators of electrification.

This analysis expands the utility of depolarization streaks to anticipate lightning potential and identify regions with active non-inductive charging (e.g., Saunders et al., 2006; Takahashi, 1978) within the cloud. Additionally, these results extend electric field measurements to winter systems to better characterize the global electric circuit (Mach et al., 2011).

## 2. Data and Methods

### 2.1. Aircraft Instrumentation

The IMPACTS field campaign utilized two aircraft platforms to study winter cyclone structure: NASA's ER-2 high altitude aircraft, and NASA's P-3 Orion aircraft (McMurdie et al., 2020). This analysis primarily utilizes observations from the NASA ER-2 aircraft (Hobbs et al., 2020) as it was equipped with a set of electric field sensing instruments called the Lightning Instrument Package (LIP) (Mach et al., 2005, 2010, 2011, 2020; Bateman et al., 2007). Additional in situ probe data from the NASA P-3 Orion (Yang-Martin & Bennett, 2020) will be used to characterize hydrometeor types and the microphysical environment within regions where active electrification is observed.

#### 2.1.1. Lightning Instrument Package

LIP consists of seven rotating vane electric field mills located at various locations on the ER-2 aircraft to observe the total vector electric field and vector electric field ( $E_x$ ,  $E_y$ ,  $E_z$ ) generated by clouds and storms as well as rapid changes in electric field due to lightning occurrence (Figure 1). LIP measures the vector electric field in the atmosphere and the charge induced on the aircraft using the processing and calibration technique in Mach and Koshak (2007). The individual laboratory dynamic range for the mills is  $\pm 1.9 \text{ V m}^{-1}$ – $1.1 \text{ MV m}^{-1}$ .

Properly calibrated on the aircraft, LIP can reliably measure fields lower than  $1 \text{ V m}^{-1}$ . Effects on the derived vertical electric field due to aircraft charging are generally 5% or less, with a maximum upper error of 10% (Mach et al., 2009). Both aircraft relative and Earth relative frameworks are determined, and the total electric field magnitude is then computed from the vector components, and the electric fields are observed from the ER-2 flight level of approximately 20 km.

### 2.1.2. Advanced Microwave Precipitation Radiometer

AMPR is a passive microwave instrument that operates at four frequencies: 10.7, 19.35, 37.1, and 85.5 GHz (Spencer et al., 1994). Calibrated brightness temperatures ( $T_B$ ) are produced as the instrument measures scattering and emission from precipitation-size ice, liquid water, and water vapor as the instrument flies above cloud top aboard NASA's ER-2 aircraft. AMPR uses two orthogonal mixed-polarization channels per frequency (A and B), and performs a  $90^\circ$  cross-track scan every 2–3 s during flight. The minimum surface footprint from the 20-km altitude of the ER-2 aircraft ranges from 640 m for the 85.5-GHz channels to 2.8 km for the 10.7- and 19.35-GHz channels. Of particular interest for this study are the 85.5-GHz channels due to their sensitivity to water vapor, clouds, and small ice, as well as, the 37.1-GHz channels, which are sensitive to smaller ice sizes (Battaglia et al., 2016; Heymsfield et al., 1996; Spencer et al., 1994).

### 2.1.3. The ER-2 Aircraft X-Band Doppler Radar

EXRAD is a dual-beam radar which operates at a frequency of 9.6 GHz (Battaglia et al., 2016; Emory et al., 2015; Heymsfield et al., 2020). EXRAD measures profiles of reflectivity and Doppler velocity using a fixed nadir antenna and a second antenna that scans conically covering approximately a 20-km swath. EXRAD is ideal for winter weather observations, particularly in locating bright band features associated with the transition from ice to water within the cloud (e.g., Austin & Bemis, 1950; Battan, 1973; Giangrande et al., 2016; Kumjian et al., 2016). Both nadir scans and horizontal reflectivity generated by EXRAD were used in this analysis.

### 2.1.4. The P-3 Orion Observations and In Situ Probes

NASA's P-3 Orion was used in the IMPACTS campaign to capture the in situ microphysics of clouds within winter storms. This study utilizes the P-3 navigation data set which incorporates position, altitude, speed, saturation vapor pressure with respect to ice, and relative humidity measured directly from the aircraft (Yang-Martin & Bennett, 2020). Supersaturation was computed by subtracting 100% from the measured relative humidity values from the P-3. Additional information was gathered from the host of microphysical probes on the P-3 aircraft to understand liquid water content (LWC), ice water content (IWC), supercooled liquid water, and cloud particle distributions.

The Stratton Park Engineering Company's two-dimensional stereo probe (2D-S) and Hawkeye Cloud Particle Imager (CPI) were used for near collocated in situ measurements of cloud properties to compare with the ER-2 instrumentation during IMPACTS (Bansemmer et al., 2020). The 2D-S probe consists of two 128-element diode arrays that record images of particles with a spatial resolution of 10 microns per pixel. The two-element diode arrays take images in the vertical and horizontal orientations. These images are then used to compute information regarding particle size distributions (i.e., concentration, mean diameter, etc.) as well as derived bulk IWC from particle diameters between 20 microns and 3 centimeters (Lawson et al., 2006).

The University of North Dakota (UND) Cloud Droplet Probe (CDP) was used to measure LWC (Delene & Poellot, 2020). The CDP measures cloud droplet concentration and size in the range of 2–50 microns based on Mie scattering principles. Previous work with probes similar to the CDP indicates that the CDP type measurement is preferred in the mixed phase environment because it has smaller biases than the King LWC when in the presence of ice (Cober et al., 2001; Lance et al., 2010). Tests by UND indicate that the CDP probe has measurement error  $<0.01 \text{ g m}^{-3}$  in the mixed phase environment. A 30-second running average and one-second instantaneous LWC values were examined from the CDP to compare with other instrumentation.

Thus, the Rosemount icing detector (RICE) was used to observe the presence of supercooled liquid water during IMPACTS. RICE is an oscillation probe that is, 6.35 mm in diameter by 2.54 cm in length (Heymsfield & Miloshevich, 1988). When supercooled liquid water accretes on the instrument, the vibrational

frequency of probe decreases from 40 kHz, and the decrease in vibrational frequency is a function of the amount of supercooled liquid water accreted on the probe. Once the ice accretion reaches 0.5 mm of ice, a heating cycle of 5 s is activated to melt the ice, and then a cool down period ensues for another 5–10 s so ice accretion can occur again (Bansemer et al., 2020).

The Hawkeye CPI is similar to the 2D-S probe in that it takes images of particles; however, the CPI instrument is classified as a high-resolution imager with a spatial resolution of 2.3 microns per pixel (Bansemer et al., 2020). As a result of the high spatial resolution, particle size distribution characteristics are not derived from CPI imagery. One-minute frame summaries were utilized to provide a qualitative view of the types of hydrometeors observed during coordinated ER-2 and P-3 overpasses. A known ice shattering effect is present within these data as very small ice pieces of larger crystals and aggregates break off as they ice hydrometeors enter the probe intake (Bansemer et al., 2020).

IWC, saturation levels, and image information from each instrument were pulled directly from the IMPACTS data set with the field catalog provided to the Global Hydrology Resource Center (GHRC). This information is all found within Bansemer et al. (2020).

## 2.2. Ground-Based Radar Data

Radar data from the ground-based Next-Generation Radar network were acquired from the National Center for Environmental Information (NCEI) Level-II radar archive (<https://www.ncei.noaa.gov/>). Horizontal radar reflectivity,  $Z_{DR}$ , correlation coefficient ( $\rho_{HV}$ ), differential phase ( $\varphi_{DP}$ ), and the Level-III derived quantity specific differential phase ( $K_{DP}$ ) computed using the operational NWS method (Reimel & Kumjian, 2020) were utilized to characterize the structure of the precipitation features within the winter cyclones. Radar data were visualized and synthesized through the Python Atmospheric Radiation Measurement Radar Toolkit (Helmus & Collis, 2016) and Gibson Ridge Software analysis packages.

Ground-based radar data were used to identify the presence of depolarization streaks in  $Z_{DR}$  and perform limited hydrometeor identification for cases where in situ aircraft observations were present.  $K_{DP}$  and  $\varphi_{DP}$  were utilized to separate regions with larger aggregates from smaller IC because smaller IC generate negative  $K_{DP}$  values when they are vertically aligned in the cloud's electric field (e.g., Hubbert et al., 2014; Kennedy & Rutledge, 2011; Kumjian, 2013; Ryzhkov & Zrnić, 2007; Thompson et al., 2014). Data from the Level-3 hydrometeor classification algorithm from the NCEI radar archive were used to identify the most likely hydrometeors in the region of electrification and at the flight level of the P-3 aircraft. These archived data were used because they are the operational HID algorithm for the National Weather Service. The algorithm uses fuzzy logic to deduce the most likely hydrometeor present in the radar volume based on the available polarimetric measurements (e.g., Heinselman & Ryzhkov, 2006; Liu & Chandrasekar, 2000; Straka et al., 2000; Vivekanandan et al., 1999). The algorithm has 10 classification categories, plus an unknown, and a range folded category. Data were displayed using UCAR/Unidata's Integrated Data Viewer (Unidata, 2021). Of specific interest for this study were the locations of IC, graupel/rimed hydrometeors, dry snow, wet snow, and rain (RA). A summary of polarimetric ranges for hydrometeors in winter precipitation which contribute to HID algorithms was captured in Thompson et al. (2014).

## 3. Total Electric Field Magnitude Observations From the 2020 Campaign

The ER-2 flew seven missions over winter cyclones in 2020, totaling 46.6 h of flight time. Three flights were to observe winter cyclones in the Northeast US, two flights were for cyclones in the Midwest US, and one flight captured a winter cyclone approximately 200 km off the Coast of North Carolina (Figure 2). The flight on 18 January was aborted before reaching the area of interest (AOI), and thus electric field data were not observed near the target of Central New York.

In general, total electric field magnitude above the winter clouds were observed to be mostly less than  $10 \text{ V m}^{-1}$  (Figure 2). The most temporally persistent total electric field magnitude above  $10 \text{ V m}^{-1}$  was in the sortie off of the Mid-Atlantic Coast on February 1, 2020, peaking around  $30 \text{ V m}^{-1}$  once the ER-2 was on station (Figure 2d). Also notable are the sharper, less temporally persistent, peaks in electric field during the February 5, February 7, and February 27 intensive observing periods (Figures 2e, 2f, and 2h). Peak electric

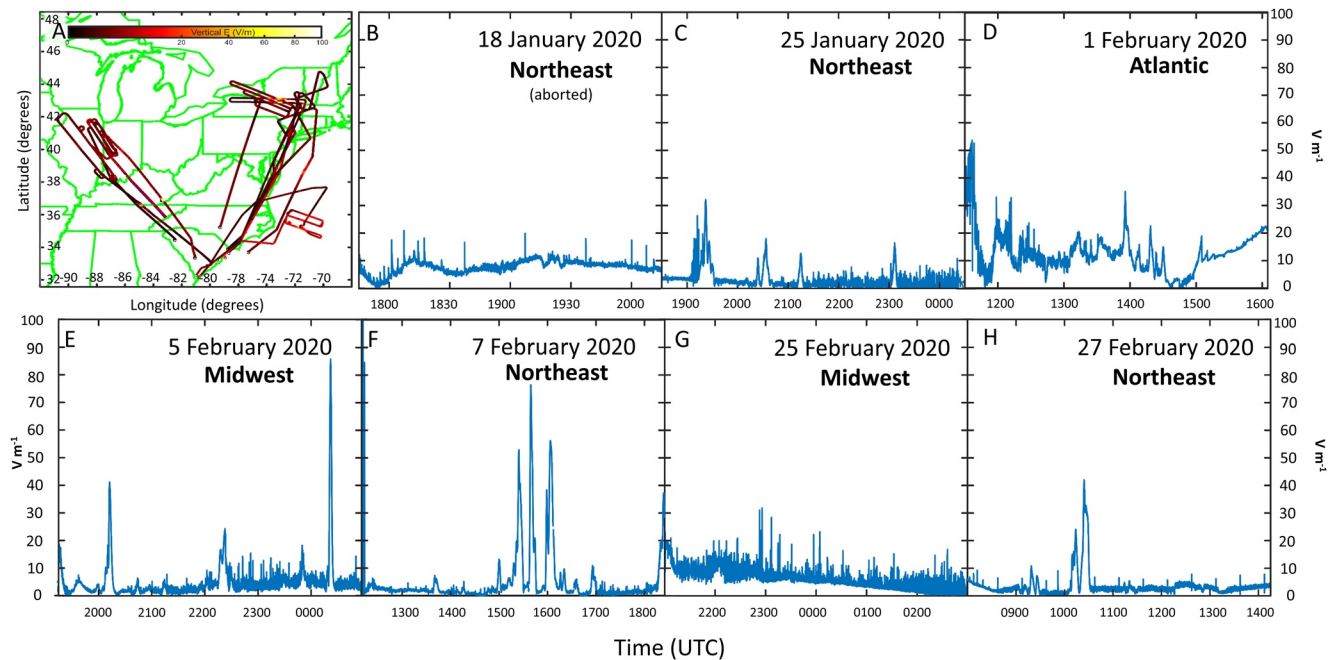


**Figure 2.** A summary of observed total electric field magnitude during the 2020 Investigation of Microphysics and Precipitation for Atlantic Coast-Threatening Snowstorms field campaign deployment. Total Electric field is represented in blue ( $V m^{-1}$ ) and the red lines indicate the aircraft paths of the ER-2 during the seven flight missions.

fields while over the AOI were observed between 40 and 70  $V m^{-1}$ . Outside of the transit portions of these flights (e.g., Figure 2b), no lightning was observed while the aircraft was on station.

Three case studies are presented to illustrate the variability in electric field and cyclone structure. The goal of these different case studies is to characterize electric fields in winter cyclones that do not generate active lightning. Three land-based missions are examined in detail in the sections below to highlight differences in electrical structure over the Midwest and Northeast.

### 3.1. February 5–6, 2020

The February 5–6, 2020 mission flew to the Midwest (Figures 2a and 2e) to sample a weak cyclone with a distinct RA/snow transition zone as the storm moved across Illinois and Indiana. During this mission, electric fields were observed exclusively within regions where bright band and convective elements were observed with EXRAD and ground-based radars. The strongest fields observed during the mission occurred on the out and back legs of the flight, and total electric field magnitudes below 5  $V m^{-1}$  were observed during overpasses where snow was reported at the surface (not shown). P-3 data were not available for periods with strong electric fields observed as both aircraft were in transit to the AOI or returning to base.

Starting around 2000 UTC February 5, the ER-2 encountered multicellular convection across northeastern Tennessee with a bright band observed just below 4 km (Figure 3). Observed total electric field magnitudes were less than 5  $V m^{-1}$  until 2112 UTC February 5, when they rose to 40  $V m^{-1}$ . Reflectivity from EXRAD and the WSR-88D radar at Morristown, Tennessee (KMRX) indicated values between 40 and 45 dBZ around this period of enhancement (Figures 3a and 3c). Additionally, enhancements in  $Z_{DR}$  between 0 and 2 dB were observed above the freezing level in the area that the ER-2 overflow, and depolarization streaks were observed just to the southwest of the aircraft track (Figures 3b and 3d). AMPR indicated  $T_B$  between 240 and 250 K in the 85-GHz (A) channel (left edge vertically polarized transitioning to right edge of swath horizontally polarized), with the strongest signatures just to the left of the swath.

Around 2345 UTC February 5, the ER-2 began its return trip to Hunter Army Airfield. During this return leg, two distinct areas of electrification were observed by LIP: 2350 UTC 5 February to 0005 UTC February

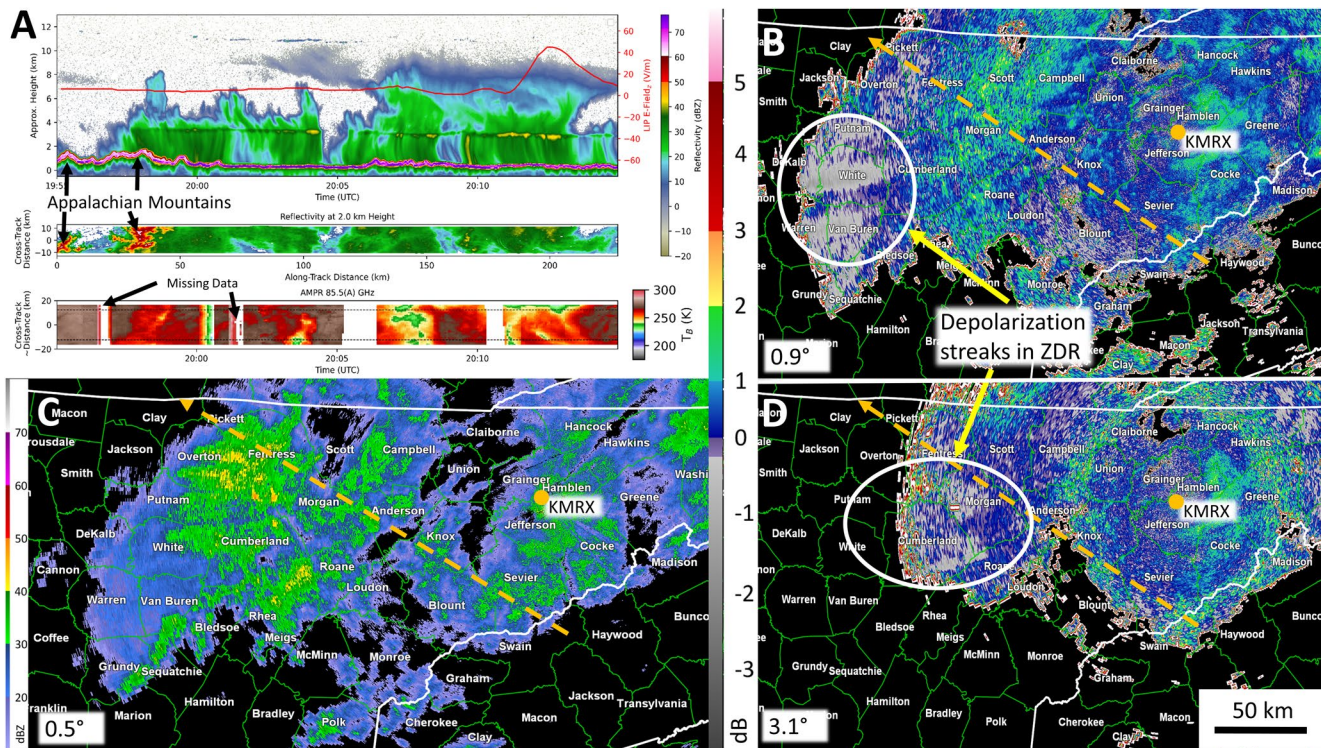


**Figure 3.** A four panel image of ER-2 based EXRAD (Panel A, top and middle), vertical electric field magnitude from LIP (red line top Panel A), AMPR (bottom Panel A), and WSR-88D radar measurements from KMRX at 2,004 UTC on February 5, 2020. The black dashed lines in the AMPR plot in Panel A indicate the swath width of the EXRAD data. Panels B and D are differential reflectivity ( $Z_{DR}$ ) and Panel C is horizontal reflectivity at elevation angles listed in the bottom left of the subplot. The aircraft track and direction are represented by the arrow at the tip in Panels B, C, and D, and the radar location is represented by the orange dot.

6 (Figure 4a) and 0010–0025 UTC on February 6 (Figure 4b). Both time periods had common bright band features just below 3 km in the EXRAD data and the strongest total electric field magnitude was nearly  $80 \text{ V m}^{-1}$  around 0022 UTC February 6. During the 2,350–0005 UTC time frame, the highest vertical electric field magnitude observed was around  $10 \text{ V m}^{-1}$  (Figure 4a) with a total electric field near  $20 \text{ V m}^{-1}$  (Figure 2e). This was associated with reflectivity between 40 and 50 dBZ in the bright band, and AMPR 85 GHz (A)  $T_B$  between 250 and 255 K (Figure 4a). The second period of interest of 0,015–0025 UTC had convective and stratiform elements. Enhancements in the total electric field were observed when the ER-2 was nearest to a 30-km north-south oriented convective feature across extreme southeastern Kentucky (Figures 4b and 5). EXRAD indicated the 40 dBZ height reached up to 4 km in this linear system. The maximum horizontal reflectivity at 2 km from was greater than 50 dBZ, and the AMPR 85-GHz channel indicated  $T_B$  values were below 200 K (Figure 4b). Depolarization streaks were observed along the same north-south orientation of this line between 3 and 7 km nearest to the same location of the  $80 \text{ V m}^{-1}$  observed total electric field in LIP (Figures 2e, 5c, and 5d) as the ER-2 passed overhead of this linear feature. The vertical component of electric field (red line, Figure 4b) from LIP indicates net positive charge over net negative charge during this period.

### 3.2. February 7, 2020

The February 7, 2020 event was the fifth science flight targeting a winter cyclone near Albany, New York. This event was characterized by a distinct transition zone between RA and heavy snow near the Catskill Mountains. The ER-2 aircraft made six east-west oriented transects over this system at approximately 20 km in height to characterize variability of the cloud electric fields within places observing snowfall, mixed-phase precipitation, and rainfall at the surface. Initially the observed electric fields were small ( $5\text{--}10 \text{ V m}^{-1}$ ) in flight leg 1 (1,355–1,430 UTC), flight leg 2 (1,435–1,500 UTC), and flight leg 3 (1,455–1,505 UTC) (Figures 2f

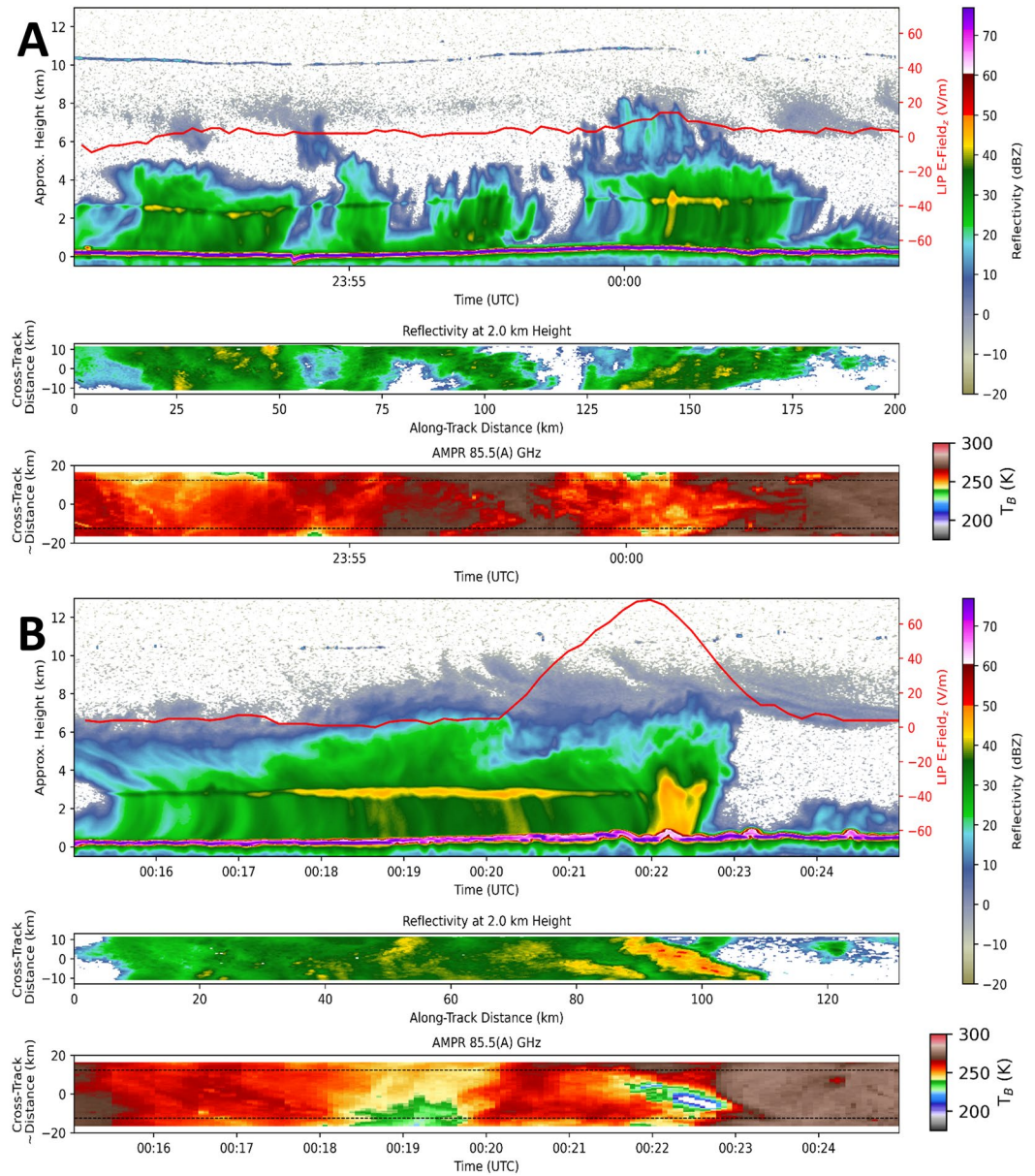


**Figure 4.** Same as Figure 3a, but for two additional times on February 5–6, 2020. Panel A is from 2,350 to 0005 UTC and Panel B is from 0010 to 0025 UTC.

and 6a). Each of these transects were in the pure snow region to the left of the bright band. The final three legs of the flight (1,507–1,525 UTC, 1,529–1,550 UTC, and 1,555–1,613 UTC) were the most electrically active during the mission. Although no lightning was observed during these three passes, total electric field magnitudes approaching  $70 \text{ V m}^{-1}$  were observed by LIP (Figure 2f).

The first indications of electric field development were around 1,522 UTC (Figure 6d). Electric field vectors pointed south, indicating generally negative charge below and to the south of the ER-2, and were on the order of  $10\text{--}20 \text{ V m}^{-1}$ . The 1,530–1,552 UTC flight leg was an east west oriented pass that moved from the transition zone near Albany to the Finger Lakes region of western New York (Figures 6e and 7). Total and vertical electric field magnitudes observed by LIP were near  $0 \text{ V m}^{-1}$  near this transition zone (1,530–1,538 UTC) as the ER-2 moved westward (Figures 2f and 7a). Then between 1,538 and 1,541 UTC the electric field magnitude increased to  $70 \text{ V m}^{-1}$  as the aircraft moved over a region of enhanced reflectivity that ranged between 30–45 dBZ (Figures 2f and 7b). The negative magnitude in the vertical electric field in

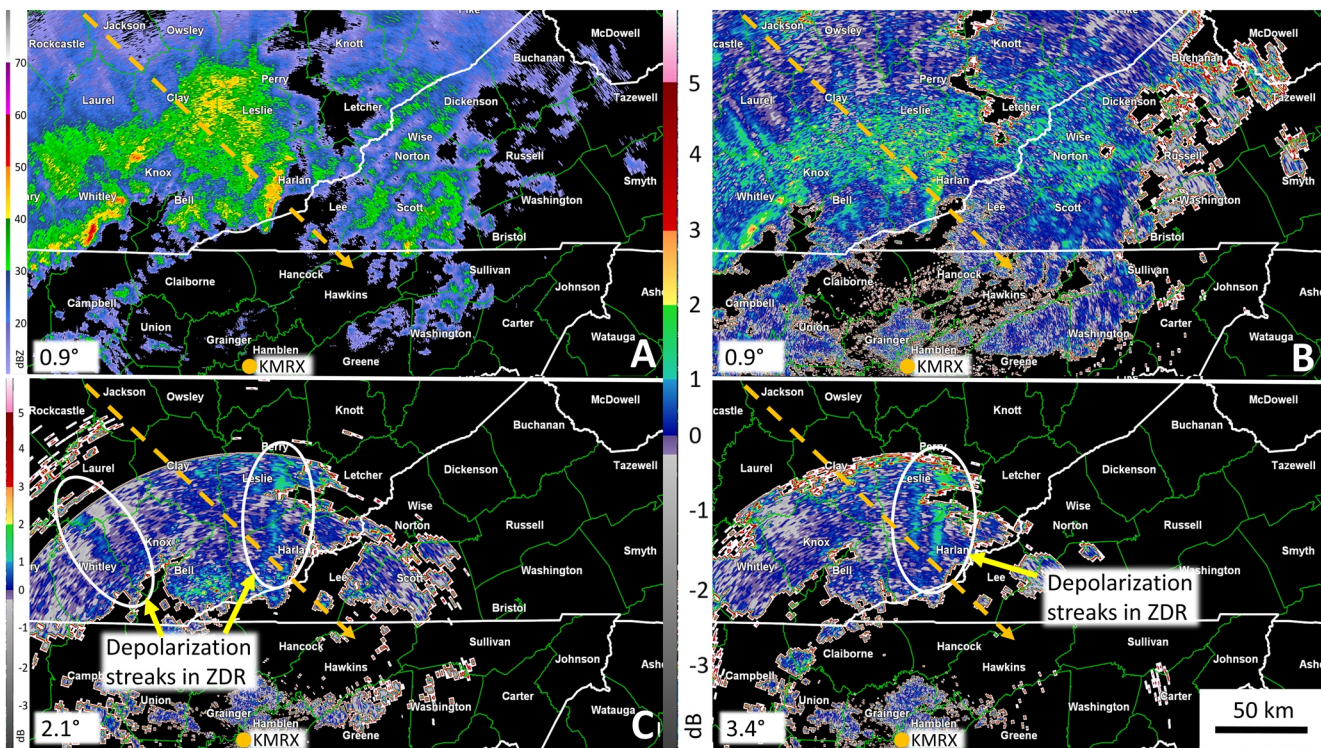


**Figure 5.** Four panel imagery of horizontal reflectivity (Panel A) and  $Z_{DR}$  (Panels B, C, and D) on February 6, 2020 at 0021 UTC from KMRX at elevation angles listed in the bottom left of the subplot. Orange dashed line with arrow is the ER-2 aircraft path and direction and the orange dot indicates the location of the KMRX radar.

Figure 7a coupled with the electric field arrows in Figure 6e indicates that the ER-2 passed just to the south of the main region of electrification.  $Z_{DR}$  was near zero for this swath of enhanced reflectivity, indicating large aggregates. Depolarization streaks in  $Z_{DR}$  were observed down-radial from the aircraft flight path at 0.5° and 0.9° elevation from KBGM at 1,540 UTC (Figures 7c and 7d). Minimum 85 GHz  $T_B$  observed by AMPR ranged from 210 to 240 K in this region of enhanced electric field. Beyond 1,541 UTC the total electric field magnitude then decreased toward 0 V m<sup>-1</sup> as the ER-2 moved away from this area of enhanced reflectivity and observed depolarization in  $Z_{DR}$ .

The 1,555 UTC leg came back eastward from the Finger Lakes toward Saratoga Springs, New York. By this time a broad region of enhanced reflectivity was noted west of Albany, between 30 and 48 dBZ (Figure 8b).  $Z_{DR}$  from Binghamton, New York (KBGM) continued to indicate multiple areas of oriented ice at 0.5° and 0.9° elevation at 1,604 UTC (Figures 8c and 8d). Vertical electric field magnitude was on the order of -30 V m<sup>-1</sup> then reversed to 50 V m<sup>-1</sup> between 1,559 and 1,604 UTC (Figure 8a) as the aircraft moved eastward toward a region of heavier precipitation. This flip in the LIP data was likely due to a field reversal observed in electric field mill data (e.g., Kitagawa & Michimoto, 1994) as LIP's field mills onboard the ER-2 moved toward regions of stronger electric field. Additional oscillations were present in the vertical electric field data between 1,605 and 1,610 UTC, with a secondary peak near 20 V m<sup>-1</sup> before dropping near 0 V m<sup>-1</sup>. The Earth-relative total field vectors in Figure 6f also indicated two regions of negative charge below and to the south of the ER-2 path. AMPR 85-GHz (A)  $T_B$  values were observed between 210 and 225 K in the region where enhanced total electric field was observed. These temperatures warmed to between 250 and 265 K as the aircraft traveled eastward into shallower precipitation and less ice scattering (Figure 8a).

The P-3 aircraft and the ER-2 made coordinated flight legs at 1,530 and 1,555 UTC to match observations from above with in situ microphysics in the cloud. The P-3 flew within the cloud between 3 and 4 km, while the ER-2 was above the cloud around 20 km in height. Because the ER-2 flew at a faster speed, the P-3 would lead the ER-2 during the early part of flight legs and the ER-2 would catch and then lead the P-3 toward the end of each flight leg. Thus, the navigation data from each aircraft (Yang-Martin & Bennett, 2020) was

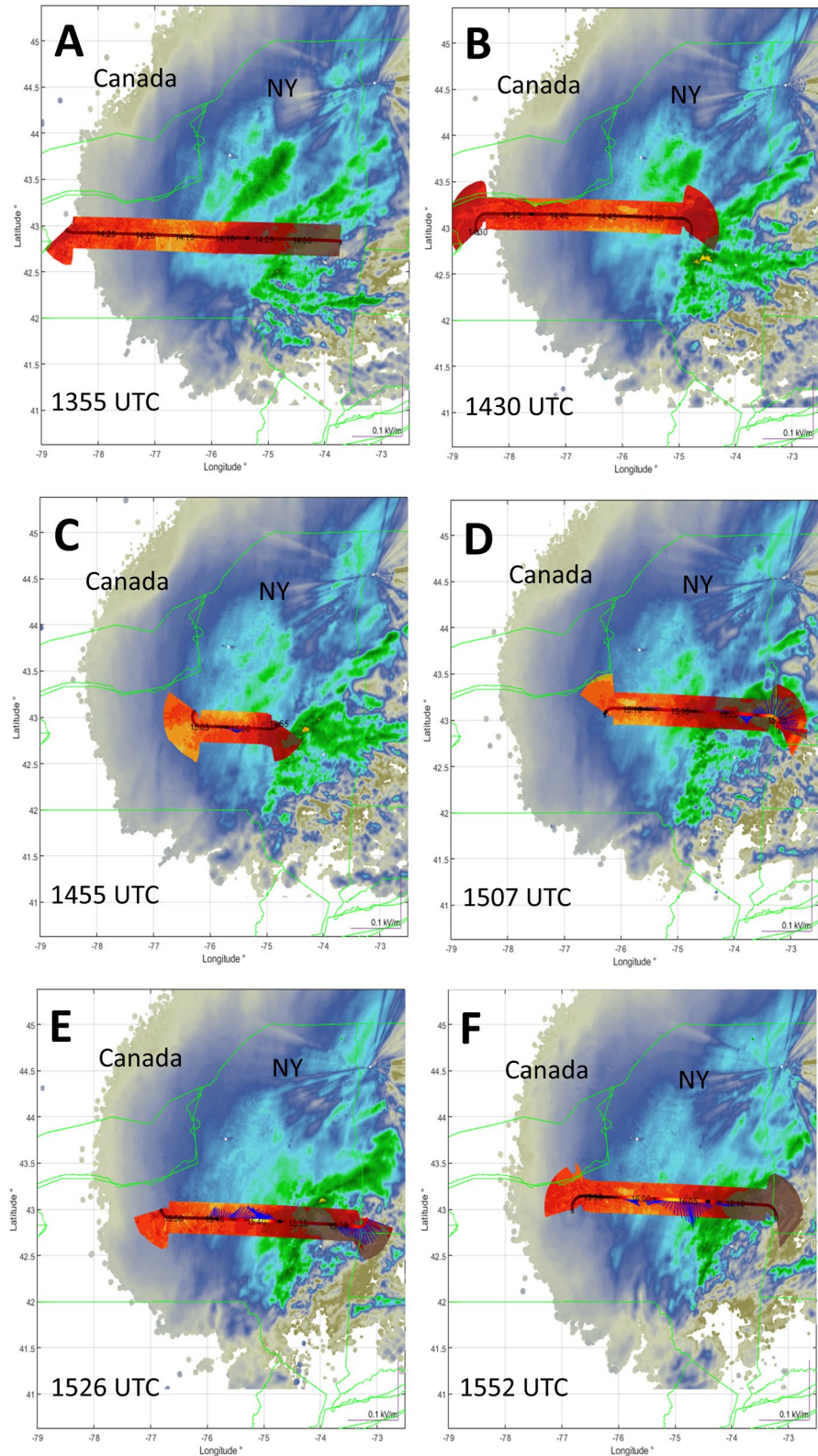


**Figure 6.** Summary plots of reflectivity (blue/green shading), AMPR (red/orange), and LIP (blue arrows in Panels D, E, F) from six flight legs between 1,355 and 1,615 UTC with the ER-2 on February 7, 2020. The blue arrows show the x and y projection of the electric field.

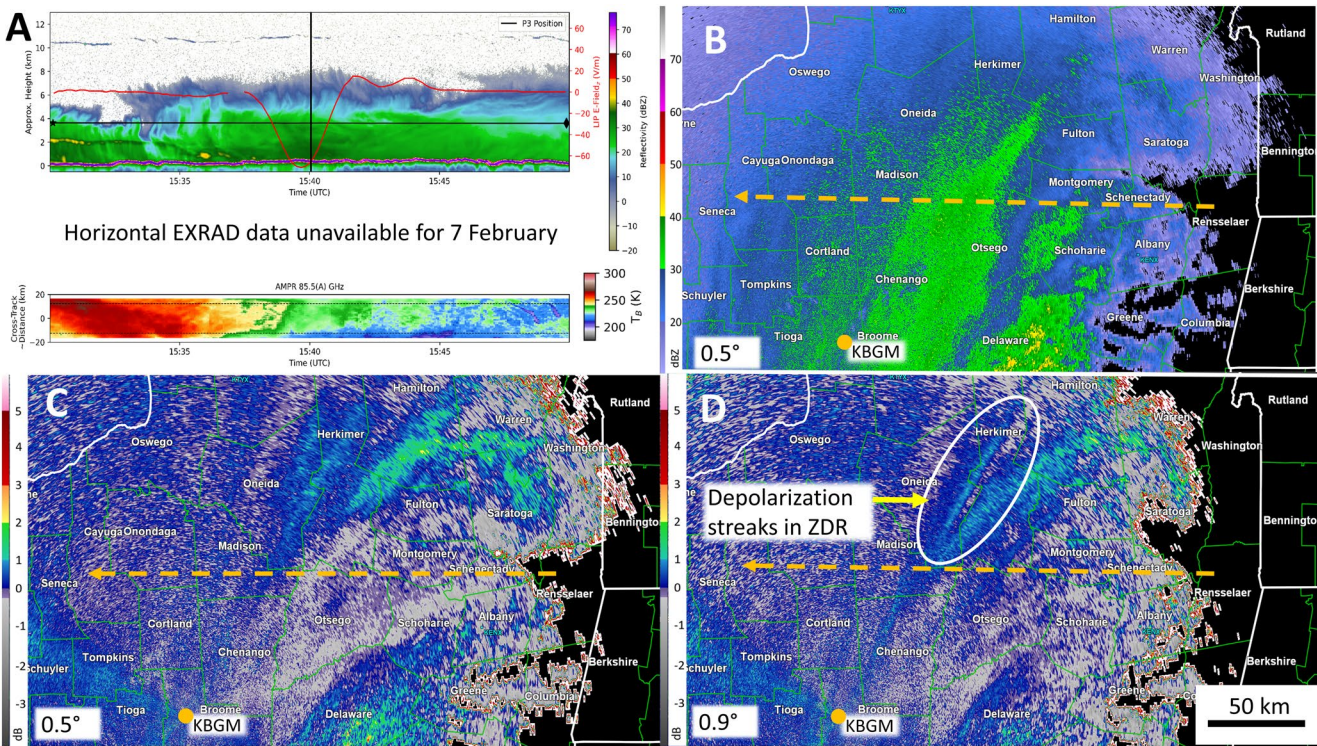


**Figure 7.** Same as Figure 3, but for a pass between 1,530 and 1,552 UTC and radar from KBGM at 1,540 UTC at elevation angles listed in the bottom left of the subplot. Horizontal reflectivity from KBGM is shown in Panel B, and  $Z_{DR}$  is shown in Panels C and D. The black horizontal line in Panel A is the height of the P-3 aircraft, and the orange dashed line is the approximate track of the ER-2 and P-3 aircraft, with the arrow providing the direction of flight. The black vertical line in Panel A indicates when the ER-2 was closest to the P-3 during the leg.

also utilized to determine the approximate position difference between each aircraft during these flight legs. Importantly, the in situ measurements aboard the P-3 were able to capture the microphysical environment in which the enhancements in total electric field were observed by LIP.

During flight leg 5 from the ER-2 (1,530–1,552 UTC) in situ observations from the P-3 provided a cross section of the microphysical environment near enhanced total electric fields. At 1,530 UTC, there was a measured decrease in the RICE frequency to 39.88 kHz between 1,530 and 1,534 UTC due to the presence of supercooled liquid water (Figure 9a). One-second LWC values from the CDP were as high as  $0.15 \text{ g m}^{-3}$ , and 30 s average LWC values were on the order of  $7.5 \text{ g m}^{-3}$ . The navigation data from both aircraft indicated the P-3 was approximately 40 km ahead of the ER-2 (P-3 location at 1,530 UTC was 42.8428234,  $-74.1424724$ , and the ER-2 was at 42.82.86593,  $-73.6393593$ ) and the ER-2's measurements lagged the P-3 by approximately three minutes. The ER-2 was over the region of measured supercooled liquid water between 1,533 and 1,536 UTC, which corresponds well to the increase in echo top heights from EXRAD.

Between 1,537 and 1,540 UTC the P-3 measured IWC near  $1 \text{ g m}^{-3}$  and supersaturation as high as 3.5% was achieved with respect to ice. RICE and CDP did not indicate supercooled liquid water or LWC during this period of maximum IWC. Saturated vapor pressure with respect to ice decreased, whereas the mean IWC and particle diameter measured by 2D-S and CPI increased. By 1,540 UTC the ER-2 closed the distance gap down to 11 km, and the measured electric field of  $70 \text{ V m}^{-1}$  corresponds well in space and time with the observed IWC and supersaturation observed in the P-3 measurements. Additionally, during this timeframe of enhanced electric field and supersaturation, the CPI imagery consisted of columns, plates, ice crystal fragments, as well as rimed aggregates (Figure 9b). As the flights continued westward, total electric fields dropped to near  $0 \text{ V m}^{-1}$  by 1,545 UTC (Figure 7a). Support for the lack of electric field after 1,545 UTC is present in the P-3 data. Non-rimed plate structures were observed in the CPI imagery at 1,548 UTC (Figure 9c), LWC was near zero, and supersaturation was not present.

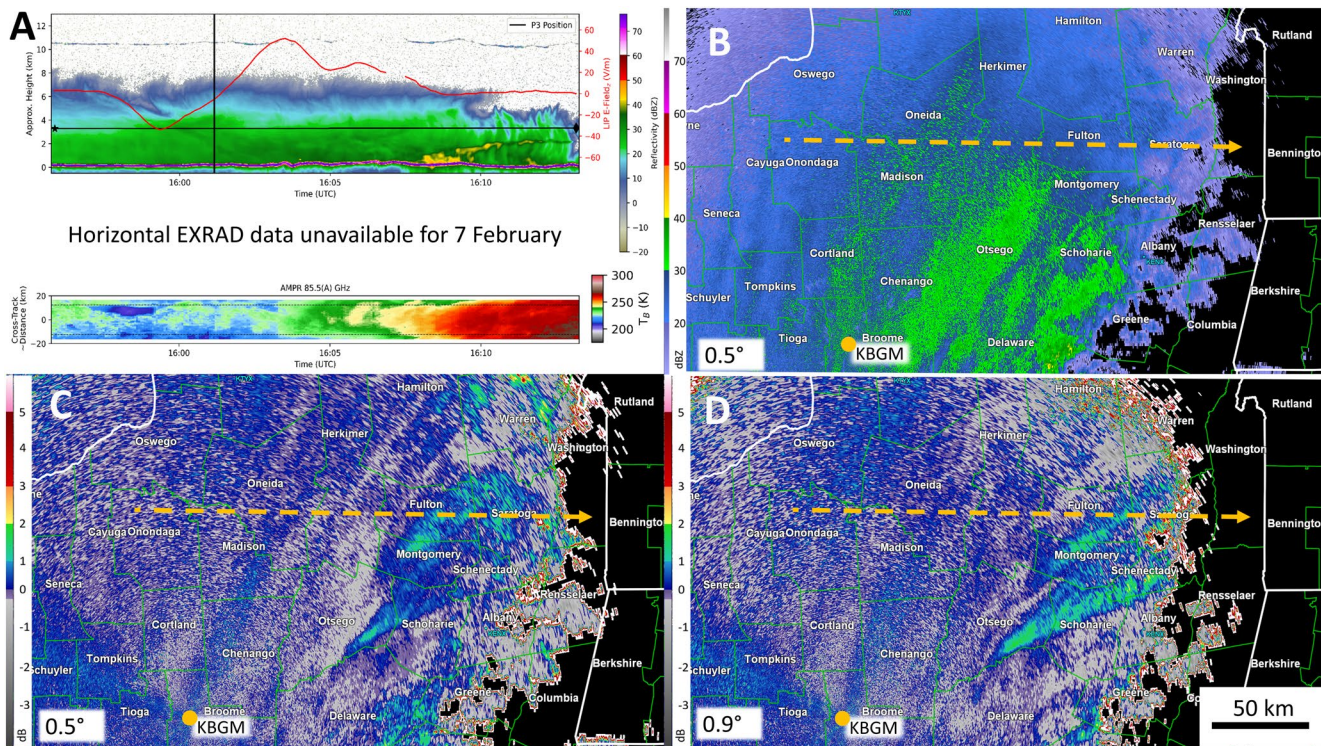


**Figure 8.** Same as Figure 7, but for an ER-2 flight leg between 1,555 and 1,615 UTC on February 7, 2020. The black horizontal line in Panel A is the height of the P-3 aircraft, and the orange dashed line is the approximate track of the ER-2 and P-3 aircraft, with the arrow providing the direction of flight. The black vertical line in Panel A indicates when the ER-2 was closest to the P-3 during the leg. Radar volume is from KBGM at 1,558 UTC.

On the last ER-2 flight leg, (1,555–1,613 UTC) supersaturation never exceeded 0.25% (Figure 10a). The IWC peaked near  $1 \text{ g m}^{-3}$  and reached minimum at nearly the same time frame as the z-direction electric field developed a positive slope between 1,559–1,604 UTC (Figures 8a and 10a). At 1,602 UTC the P-3 lagged the ER-2 by approximately 3 km, so the aircraft measurements were close in space and time. The CPI continued to monitor plate-like habits, particle fragments from ice shattering, and rimed particles in the regions of enhanced reflectivity (Figure 10b). As the ER-2 traversed over the bright band region, the vertical electric field levels decreased toward  $0 \text{ V m}^{-1}$ . RICE observed a decrease in oscillation frequency down to 39.96 kHz between 1,611 and 1,614 UTC, indicating the presence of supercooled liquid water as the P-3 traveled eastward through Eastern New York (Figure 10a). The location of measured supercooled liquid water corresponds to the ER-2 location at 1,609 UTC, where 20 dBZ echo tops observed by EXRAD transitioned from approximately 7 km down to 5 km (Figure 8a). CDP also indicated LWC in this region, with peak 30 s averages near  $0.75 \text{ g m}^{-3}$ .

An examination of the National Weather Service's level-3 hydrometeor identification algorithm (HID) using KBGM illustrated this complex microphysical environment where IC, graupel/aggregates, and the P-3 flight path. KBGM's beam height at  $0.5^\circ$  elevation over this region was approximately 3 km in height, which was close to the same flight altitude of the P-3 aircraft during the 1,530 and 1,555 UTC flight legs. At this altitude the HID algorithm indicated IC and graupel/rimed aggregates at the location where the ER-2 and P-3 were collocated (Figures 10c and 10d). There was a noted difference in the areal extent of the HID identified graupel/rimed aggregates between 1,540 and 1,602 UTC, as a smaller area of graupel was identified at 1,602 UTC versus 1,540 UTC from KBGM. After 1,615 UTC the ER-2 returned to base and coordinated flight legs with the P-3 ended.

### 3.3. February 27, 2020

The February 27, 2020 mission was located over central and western New York between 0900 and 1300 UTC. Only the ER-2 was available for this event. Four of the eight legs by the ER-2 during this mission contained

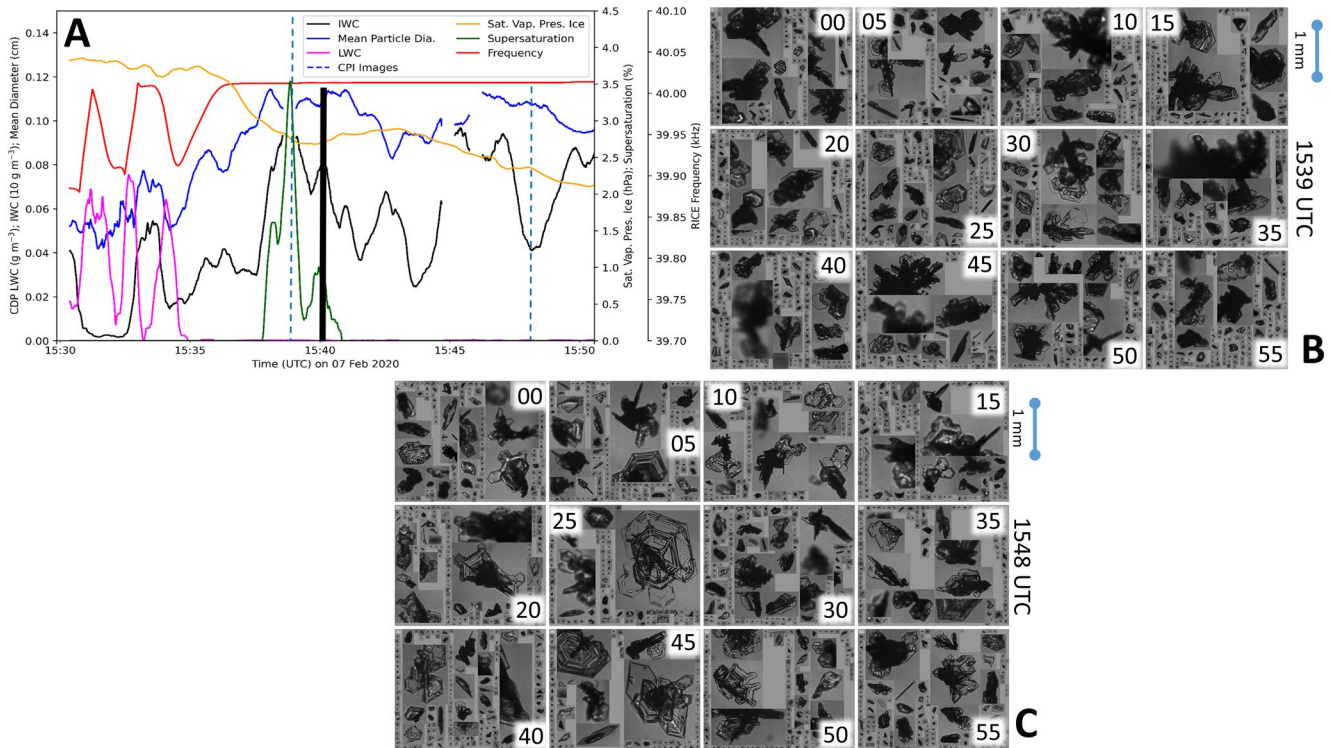


**Figure 9.** In situ measurements from the P-3, two-dimensional stereo probe, University of North Dakota Cloud Droplet Probe, and Rosemount icing detector instruments on February 7, 2020 between 1,529 and 1,552 UTC (Panel A) Hawkeye Cloud Particle Imager (CPI) images at 1,539 and 1,548 UTC (Panels B and C) provide images of the hydrometeor types during the two, one-minute periods. ice water content (IWC) values are divided by 10 to be on the same magnitude scale as the CPI measurements, thus multiply IWC by 10 to get the IWC values in g m<sup>-3</sup>. The black vertical line indicates when the ER-2 was closest to the P-3 during the leg.

total electric field observations from LIP larger than 5 V m<sup>-1</sup> and none of the enhanced fields were coincident with lightning occurrence. The largest total electric field magnitude observed was around 40 V m<sup>-1</sup> and the duration of enhanced electric field was 22 min between 1,010 and 1,032 UTC (Figures 2h and 11). The most interesting features of this event were the evolution of the electric field and depolarization streaks in Z<sub>DR</sub> from the ground-based radars.

During the first leg of the flight between 0915 and 0945 UTC, electric fields approaching 10 V m<sup>-1</sup> were observed southwest of Albany (Figures 2h and 11a). Fields were observed with reflectivity features in EXRAD that approached 7 km in height. AMPR 85-GHz (A) T<sub>B</sub> values were between 250 and 265 K in this area where LIP observed total fields above 5 V m<sup>-1</sup>. Less than 10 min after the ER-2 exited the region on its northwestern flight leg, depolarization streaks were observed in Z<sub>DR</sub> from Fort Drum, New York (KTYX) at 0.5° and 0.9° elevation near where LIP observed total electric fields above 5 V m<sup>-1</sup>, and horizontal reflectivity was between 20 and 30 dBZ (Figure 12).

The ER-2 made a northwest to southeast return flight between 0949 and 1,016 UTC (Figure 13). Electric fields observed by LIP were less than 5 V m<sup>-1</sup> through 1,005 UTC and were collocated with radar echoes that were around 4 km or lower in height. After 1,005 UTC, EXRAD indicated a deepening of the precipitation echoes up to 6 km in height. Coincidentally, KTYX observed depolarization streaks in Z<sub>DR</sub> between 128° and 148° azimuths, just west of Albany. Streaks were observed up to 4 km in elevation (not shown). Oscillations in the vertical electric field between 20 and -20 V m<sup>-1</sup> were observed by LIP as the ER-2 made an overpass over the depolarization area. AMPR 85-GHz T<sub>B</sub> observations were on the order of 250–265 K and reflectivity from KTYX at 0.5° elevation was generally less than 30 dBZ along this flight path (Figures 13a and 13c).

The final leg of interest occurred between 1,021 and 1,049 UTC, where the ER-2 made another southeast to northwest pass over central and western New York (Figure 14). Observed electric field magnitudes were between 20 and 45 V m<sup>-1</sup> as the ER-2 passed over and near the same depolarization streaks, which had

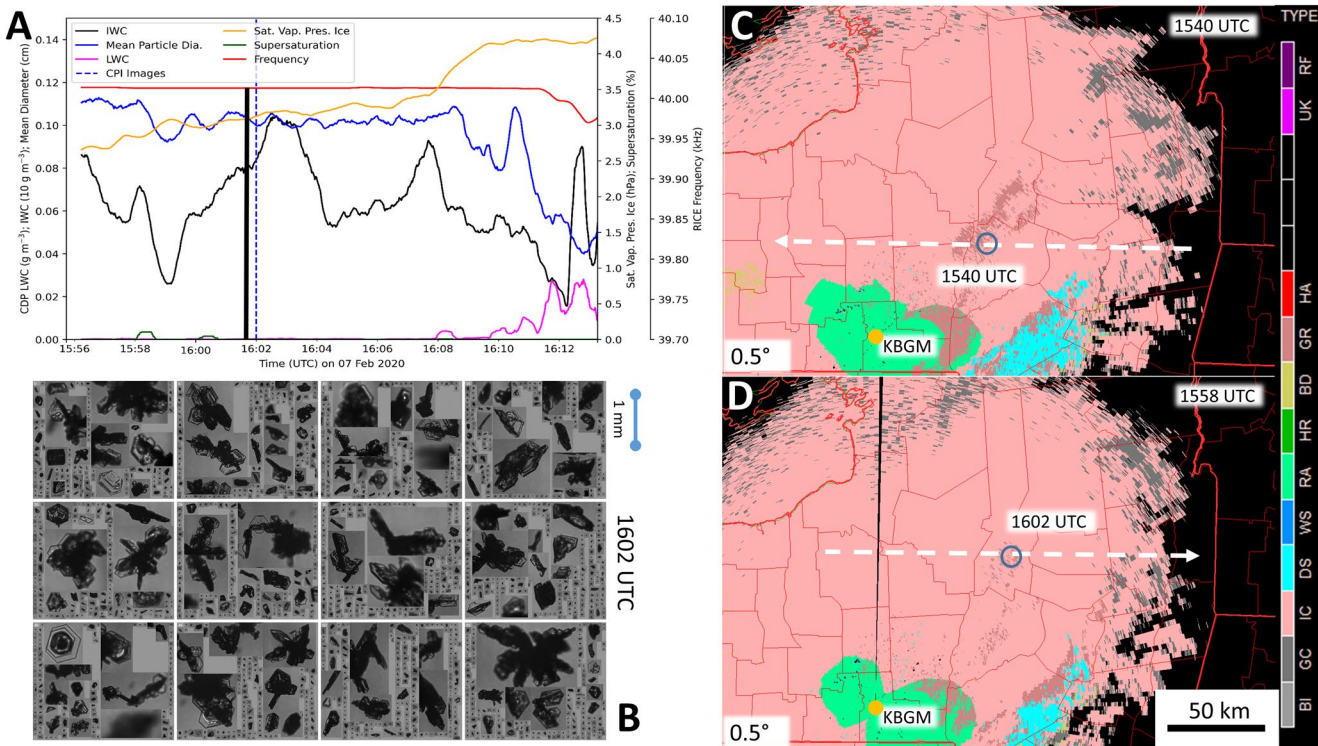


**Figure 10.** In situ measurements from the P-3, two-dimensional stereo probe, University of North Dakota Cloud Droplet Probe, and Rosemount icing detector instruments on February 7, 2020 between 1,556 and 1,614 UTC (Panel A) CPI images at 1,602 UTC (Panel B) provide images of the hydrometeor types during a one-minute period where the P-3 and ER-2 were collocated. Ice water content (IWC) values are divided by 10 to be on the same magnitude scale as the Hawkeye Cloud Particle Imager (CPI) measurements, thus multiply IWC by 10 to get the IWC values in  $\text{g m}^{-3}$ . The black vertical line indicates when the ER-2 was closest to the P-3 during the leg. Panels C and D are level 3 hydrometeor classification from the National Weather Service hydrometeor identification algorithm using KBGM at 1,540 and 1,558 UTC to correspond to the in situ observations. Abbreviations for the hydrometeor classification scale are: biological, ground clutter, ice crystals, dry snow, wet snow, rain, heavy rain, bad data, graupel/rimed aggregates, hail, unknown, and range fold. The white dashed line is the ER-2 flight path and the blue circles are the location of the in situ observations at 1,540 and 1,602 UTC.

advected 25 km to the north-northeast (Figures 2h and 14). EXRAD indicated 20-dBZ echo tops around 6 km near the strongest magnitude of  $40 \text{ V m}^{-1}$ . AMPR  $T_B$  values were between 250 and 265 K along this early portion of the track. Initial field vectors were downward and toward the right side of the ER-2 path, indicating net negative charge in the direction of the depolarization streaks between  $119^\circ$  and  $127^\circ$  azimuths (Figures 14c and 14d); however, as the ER-2 traveled westward, the vertical electric field vector reversed direction (Figure 13d), indicating positive charge below and to the right of the aircraft. Distinct depolarization streaks in  $Z_{DR}$  were not observed until 1,034 UTC by any of the three radars closest to the aircraft track (Figures 14e and 14f). After 1,030 UTC, total electric field magnitudes below  $5 \text{ V m}^{-1}$  were observed for the remainder of the flight leg.

Of the five additional flight legs that the ER-2 performed on February 27, 2020, only one observed electric fields above  $5 \text{ V m}^{-1}$ . This was the return leg between 1,053 and 1,120 UTC, where LIP measured an electric field near  $10 \text{ V m}^{-1}$ . A single depolarization streak was present from KTYX at 1,120 UTC. After this occurrence, electric field observations during the remaining flight legs were minimal, and depolarization streaks were no longer observed in the vicinity of the ER-2 flight legs through 1,300 UTC.

#### 4. Discussion

The unique combination of airborne electric field, radar, passive microwave, and in situ observations provided by the 2020 IMPACTS field campaign support theories in fundamental understanding of charging in winter clouds and the application of radar artifacts to improve lightning situational awareness.

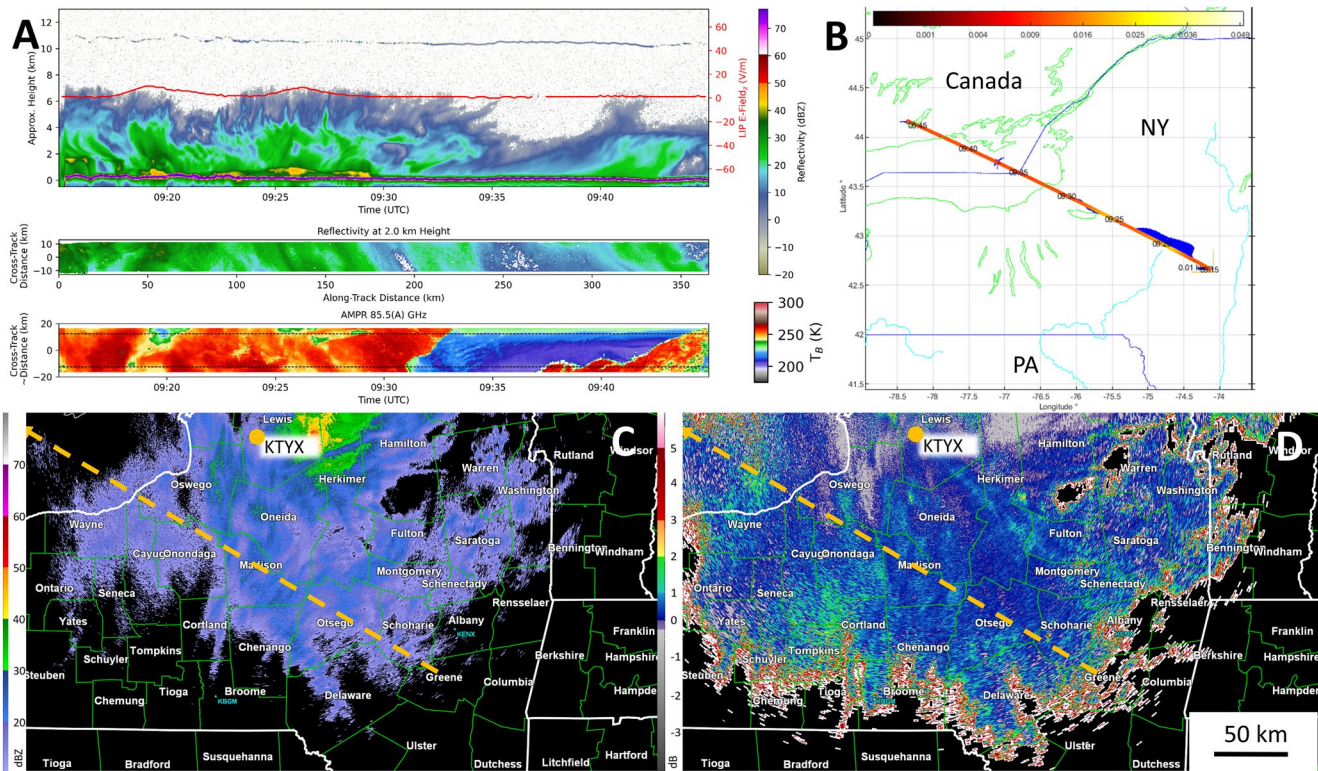


**Figure 11.** Four panel of images covering the development of Lightning Instrument Package (LIP) observed vertical electric fields on February 27, 2020. EXRAD (Panel A, top and middle), LIP (red line top Panel A), and AMPR (bottom Panel A). The black dashed lines in the AMPR plot in Panel A indicate the swath width of the EXRAD data. Panel B is the ER-2 flight track with LIP total electric field vectors (blue). Panels C and D are radar reflectivity and  $Z_{DR}$  measurements from KTYX at  $0.5^\circ$  elevation on February 27, 2020 at 0925 UTC. Orange dashed line is the aircraft path and the arrow is the direction of flight. The orange dot indicates the location of the KTYX radar.

#### 4.1. Observations of IWC, Supersaturation, and Strong Electric Fields on February 7, 2020

Leading theories on electrification of clouds require the presence of supercooled liquid water for active charge separation and electric field development (Saunders et al., 2006; Takahashi, 1978). The coordinated ER-2 and P-3 aircraft passes on February 7, 2020 provide limited but supportive evidence of the role of supercooled liquid water and IWC in electrification of winter clouds.

In the 1,530 and 1,555 UTC flight legs, the largest IWC is collocated in space with the largest electric field magnitudes measured by LIP. Even after correcting for differences in aircraft position, there is a spatial offset between supercooled liquid water measured by RICE, LWC from the UND CDP, and peak electric field strength observed by LIP. Baker and Dash (1994) and Nelson and Baker (2003) hypothesized how depositional growth favors charge separation through an exchange of mass between growing IC and graupel in the presence of supercooled water. The CPI probe indicated rimed aggregates alongside smaller IC in this region of enhanced electric field that was slightly offset from the supercooled liquid water. However, without three-dimensional information on the location of supercooled liquid water, lack of three-dimensional charge structure, and a trajectory analysis of the hydrometeors observed in CPI, it is difficult to characterize this offset beyond the aircraft observations.

There was also support for electrification within low supercooled liquid water environments which previous studies have observed (e.g., Avila et al., 2005; Dye & Bansemer, 2019; Dye & Willett, 2007; Tsenova et al., 2017). This was most apparent on the 1,555 UTC leg on February 7; where LIP measured electric field above the cloud for over 12 min without collocated supercooled liquid water observed within the cloud from the RICE instrument onboard the P-3 (Figures 8–10). An upper air sounding at 1,500 UTC from the University of Illinois Urbana-Champaign (UIUC) sounding team (Rauber et al., 2020) near Syracuse, NY (43.103,  $-76.193$ ) indicated there is a warm nose of above freezing temperatures around 300 m in depth,

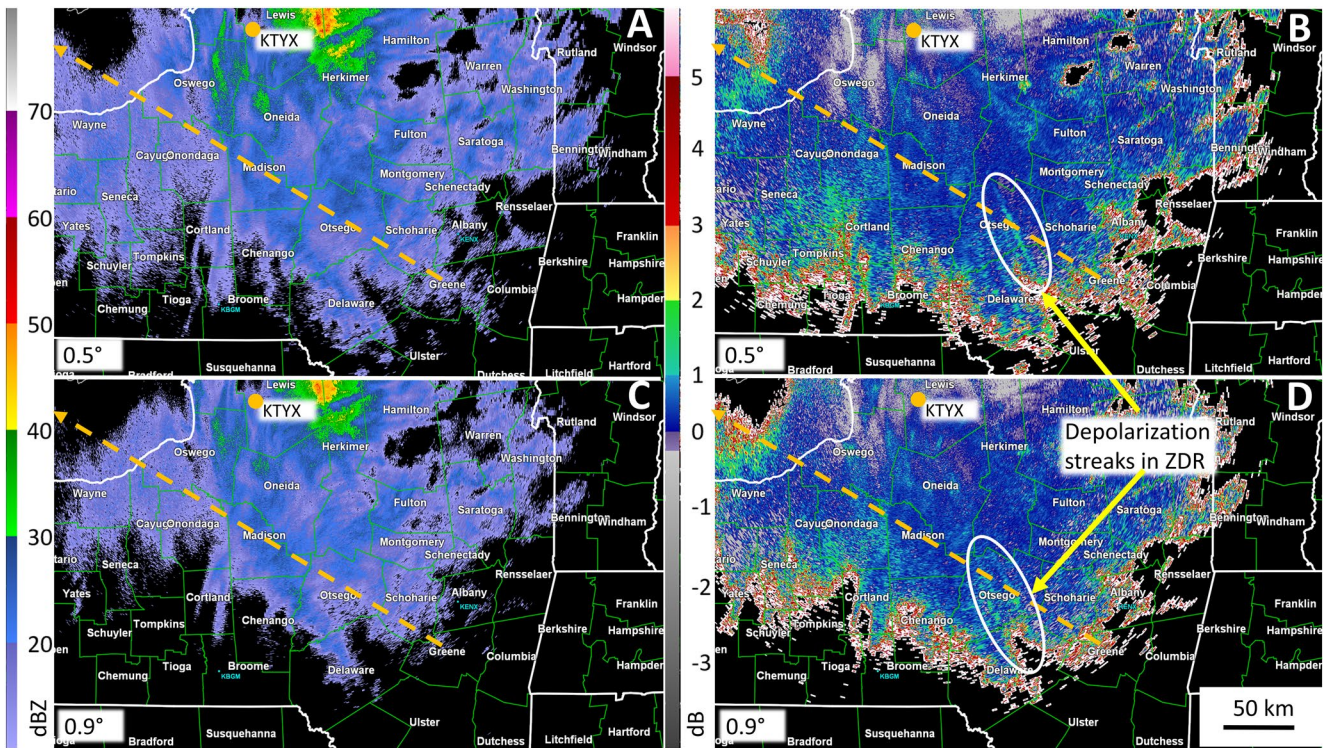


**Figure 12.** Four panel image of reflectivity (Panels A and C) and  $Z_{DR}$  (panels B and D) on February 27, 2020 at 0934 UTC from KTYX at elevation angles listed in the bottom left of the subplot. Panels A and B are at  $0.5^\circ$  elevation, and Panels C and D are at  $0.9^\circ$  elevation. Orange dashed line is the aircraft path and the arrow is the direction of flight. The orange dot indicates the location of the KTYX radar.

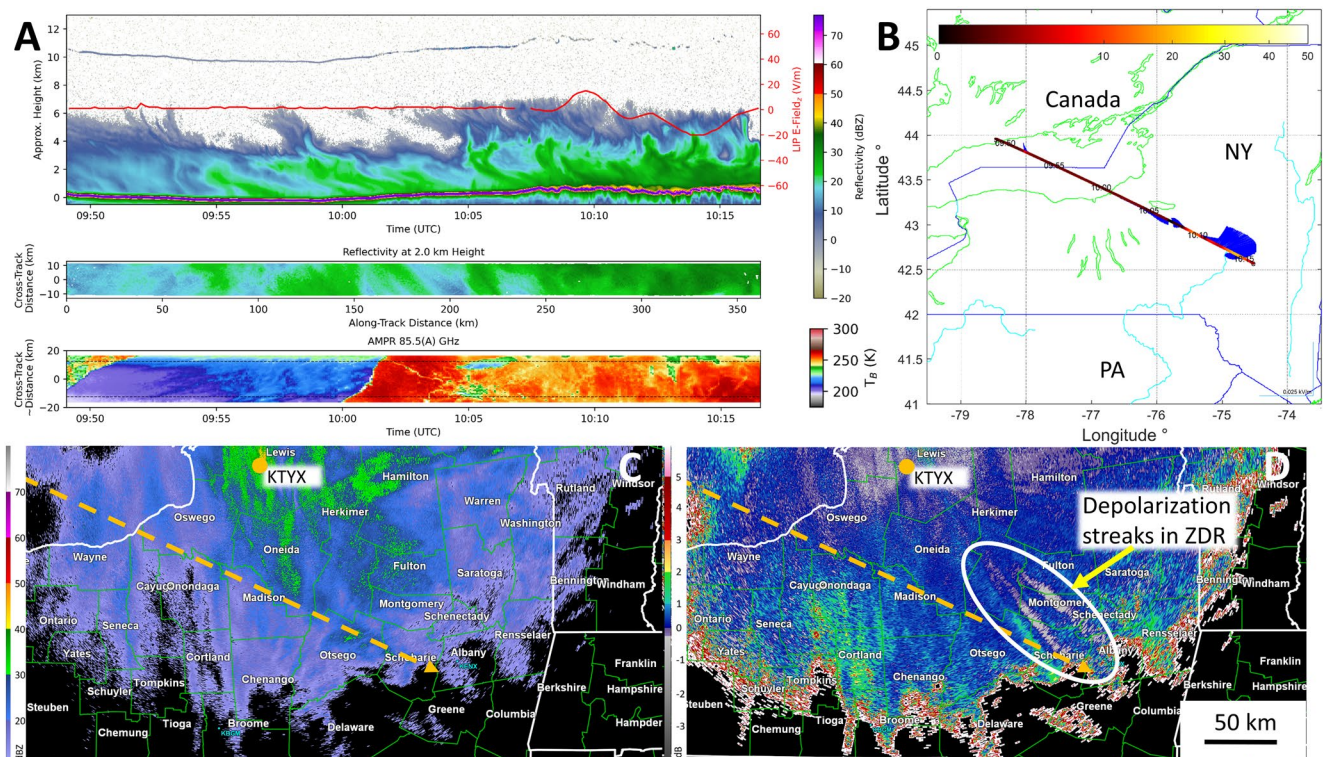


**Figure 13.** Same as Figure 11 but for an ER-2 flight leg between 0949 UTC and 1,016 UTC on February 27, 2020.

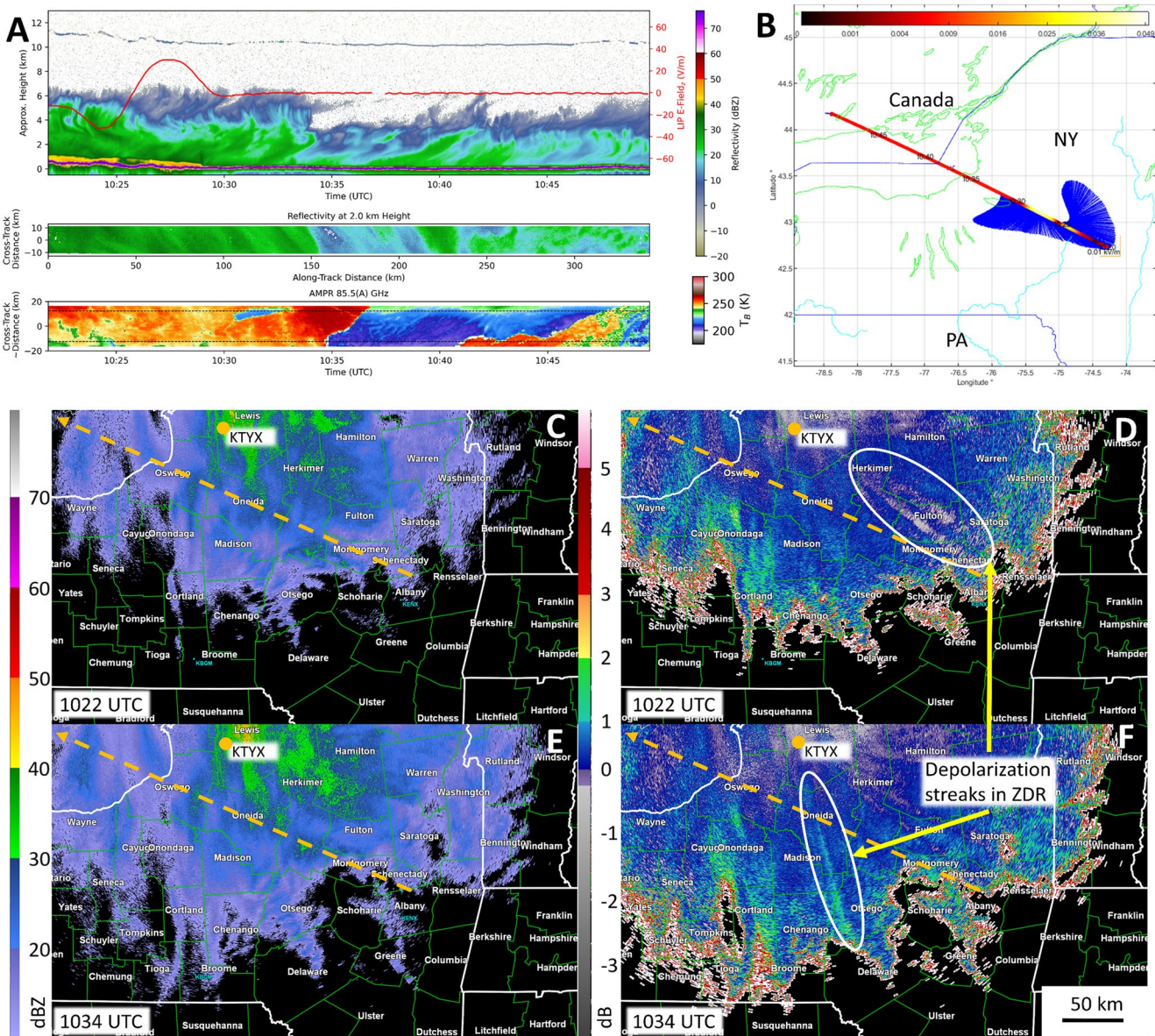


**Figure 14.** A six panel image of an ER-2 flight leg between 1,021 and 1,049 UTC on February 27, 2020. Panel A is the EXRAD, LIP, and AMPR information as in Figure 3a. Panel B is the flight track and vertical electric field vectors from LIP during the overpass. Panels C–F are radar reflectivity from KTYX at 1,025 UTC (Panels C and D) and 1,034 UTC (Panels E and F) at 0.5° elevation. In Panels C–F the orange dashed line is the aircraft path and the arrow is the direction of flight. The orange dot indicates the location of the KTYX radar.

with temperatures as high as 3°C at 1.5 km in height (Figure 15). Critical temperature thresholds of –10 and –20°C used for understanding the most robust mixed phase region were at 3.7 and 5.5 km, respectively (e.g., Saunders et al., 2006; Takahashi, 1978). The temperature at the flight level of the P-3 was around 25°C, with measured LWC from the CDP probe less than 0.07 g m<sup>-3</sup>. This indicates that the sign of the charge transferred to the rimer was likely negative and that the charge structure was a main positive layer over a main negative layer (Saunders et al., 2006; Tsenova et al., 2017).

Without the presence of lightning or electric field soundings, this study cannot confirm the full three-dimensional electrical structure of the cloud. Previous work with lightning in heavy snowfall within the United States shows a predominance of negative cloud-to-ground lightning flashes, and positive over negative charge structures (e.g., Harkema et al., 2019; Market & Becker, 2009; Schultz et al., 2018). Limitations in the



#### 4.2. Variance in the Electric Field in Winter Systems

During the 2020 IMPACTS flights using the ER-2 at an altitude near 20 km, variability of the local cloud electric field was present within the LIP measurements, indicating multiple regions of charge in two snow-producing systems (e.g., Figures 7, 8, and 12). This variability is supportive of measurements from the Sea of Japan and Utah, where horizontal and vertical variability of charge structure was observed within winter systems. While no lightning was observed during these three IMPACTS flights, the implications of variability of electric field indicates that controls on flash size relative to kinematic and microphysical structure observed in warm-season thunderstorms likely extend to winter systems (e.g., Bruning & MacGorman, 2013). There is evidence of this control on flash size in previous lightning studies, where a continuum of flash sizes has been observed within winter cyclones (e.g., Schultz et al., 2018; Harkema et al., 2019). The heights of the cloud as observed by EXRAD are similar to other studies, where cloud top heights are below 10 km (Figures 7, 8, 11, and 12; Rauber et al., 2014; Schultz et al., 2018). However, with limited data from the 2020 IMPACTS campaign, additional observations of electric fields in winter storms are necessary to understand this variability in electrical structure within winter storms to build upon the work of Brook et al. (1982), Kitagawa and Michimoto (1994), and Rust and Trapp (2002).

#### 4.3. Application of LIP and Radar Depolarization in $Z_{DR}$ for Lightning Safety

Winter lightning has been known to cause injuries, fatalities, and damage (e.g., Curran et al., 2000; Holle et al., 1997). Traditional lightning safety metrics may not be applicable for winter storms because lightning safety guidelines like the 30-minute rule (Holle et al., 1999; Stano et al., 2019) may no longer be in effect when a subsequent flash occurs due to the relatively infrequent flash rates as compared to warm-season thunderstorms. However, depolarization streaks in  $Z_{DR}$  have the potential to monitor for the risk of these infrequent lightning events. In each case study presented above, depolarization was observed near the strongest electric fields for each flight. Thus, there is potential utility of this lightning nowcasting technique to the winter weather environment. However, developing applications requires a deeper look into when the use of these signatures is needed, given that each depolarization streak observed in this study did not produce lightning but was associated with cloud electrification, and in an initial look at the Harkema et al. (2019) data set, not all lightning flashes in winter storms were accompanied by depolarization streaks in  $Z_{DR}$ .

### 5. Conclusions

Aircraft electric fields from LIP were combined with airborne, ground-based, and in situ measurements to understand microphysical conditions where cloud electrification was observed in winter storms during the 2020 IMPACTS field campaign. Key observations from this study include:

1. LIP observed electric fields were as high as  $80 \text{ V m}^{-1}$  above the systems during the seven research flights conducted in the 2020 field campaign into winter clouds.
2. X-band airborne radar data indicated 20-dBZ echo tops above 5 km in regions where electrification exceeded  $10 \text{ V m}^{-1}$ .
3. In regions where electric field magnitudes above the storms exceeded  $10 \text{ V m}^{-1}$ , 85-GHz brightness temperatures ( $T_B$ ) from an airborne radiometer were lower than 265 K, with the lowest  $T_B$  ( $\sim 210\text{K}$ ) associated with ice scattering collocated with the strongest electric field of  $80 \text{ V m}^{-1}$ .
4. Depolarization streaks in  $Z_{DR}$  were observed to be collocated with areas of total electric field magnitude greater than  $20 \text{ V m}^{-1}$  from LIP at an altitude of 20 km, indicative of ice crystal orientation in the cloud's electric field.
5. During the February 7, 2020 research flight with collocated in situ P-3 measurements, supersaturation and rimed aggregates were observed near regions of enhanced electric field and depolarization in  $Z_{DR}$ . RICE and CDP observations of LWC and supercooled water indicated spatial separation from the largest IWC and electric fields measured by LIP along the flight path. This finding corroborates the microphysical measurements of riming, LWC, and supercooled liquid water within winter cyclones in Rauber et al. (2014).

### Data Availability Statement

The IMPACTS data from UIUC Soundings, LIP, AMPR, EXTRAD, Hawkeye, RICE, 2D-S, and CPI probes used within this analysis are available online from the NASA EOSDIS Global Hydrology Resource Center Distributed Active Archive Center, Huntsville, Alabama, USA (doi: <http://dx.doi.org/10.5067/IMPACTS/DATA101>). Individual instrument locations are within the citations in the reference section. Ground based radar data from the National Weather Service WSR-88D radars was obtained from NOAA's Amazon Web Services (<https://s3.amazonaws.com/noaa-nexrad-level2/index.html>). The authors are grateful to the IMPACTS teams that collected these data that went into the analysis within the present study. The authors are also grateful for the time of three anonymous reviewers who improved and provided feedback to clarify statements made within the initial draft of this manuscript.

### Acknowledgments

The authors would like to acknowledge funding support from the NASA IMPACTS Earth Venture Mission and International Space Station Lightning Imaging Sensor Mission supported by Dr. Gail Skofronick-Jackson and Dr. Tsengdar Lee at NASA Headquarters. Coauthor Harkema would like to acknowledge funding from NASA's Future Investigators in Earth and Space Science and Technology program through grant number 80NS-SC20K1623. The team also appreciates the work of Dr. Barry Lefer and Dr. Walt Petersen for discussions to bring the Lightning Instrument Package into the NASA ER-2 instrument suite post selection of the IMPACTS EVS, and the support from Dr. Lynn McMurdie for acknowledging the importance of the electric field measurements and writing letters of support. The team appreciates the pilots, ground crews, forecasters, aircraft logistics, and mission scientists for their hard work in making sure the aircraft and instrument teams were supported and quality data were collected during each of the missions. The team would also like to recognize the hard work of Michael Stewart, Scott Podgorney, and David Corridor at UAH in preparing LIP for the 2020 IMPACTS field campaign.

### References

Adhikari, A., & Liu, C. (2019). Remote sensing properties of freezing rain events from space. *Journal of Geophysical Research: Atmospheres*, 124, 10385–10400. <https://doi.org/10.1029/2019JD030788>

Austin, P. M., & Bemis, A. (1950). A quantitative study of the bright band in radar precipitation echoes. *Journal of Meteorology*, 7, 165–171. [https://doi.org/10.1175/1520-0469\(1950\)007<0145:aqsofb>2.0.co;2](https://doi.org/10.1175/1520-0469(1950)007<0145:aqsofb>2.0.co;2)

Avila, E. E., Saunders, C. P. R., Bax-Norman, H., & Castellano, N. E. (2005). Charge sign reversal in irregular ice particle-graupel collisions. *Geophysical Research Letters*, 32, L18101. <https://doi.org/10.1029/2004GL020761>

Baker, M. B., & Dash, J. G. (1994). Mechanism of charge transfer between colliding ice particles. *Journal of Geophysical Research*, 99, 10621–10626.

Bansemer, A., Delene, D., Heymsfield, A. J., O'Brien, J., Poellot, M. R., Sand, K., & Sova, G. (2020). NCAR Particle Probes IMPACTS, dataset available online from NASA GHRC DAAC. <http://dx.doi.org/10.5067/IMPACTS/PROBES/DATA101>

Bateman, M. G., Rust, W. D., Smull, B. F., & Marshall, T. C. (1995). Precipitation charge and size measurements in the stratiform region of two mesoscale convective systems. *Journal of Geophysical Research*, 100, 16341–16356. <https://doi.org/10.1029/95JD01280>

Bateman, M. G., Stewart, M. F., Blakeslee, R. J., Podgorny, S. J., Christian, H. J., Mach, D. M., et al. (2007). A low-noise microprocessor-controlled, internally digitizing rotating-vane electric field mill for airborne platforms. *Journal of Atmospheric and Oceanic Technology*, 24, 1245–1255. <https://doi.org/10.1175/JTECH2039.1>

Battaglia, A., Mroz, K., Lang, T., Tridon, F., Tanelli, S., Tian, L., & Heymsfield, G. M. (2016). Using a multiwavelength suite of microwave instruments to investigate the microphysical structure of deep convective cores. *Journal of Geophysical Research: Atmospheres*, 121, 9356–9381. <https://doi.org/10.1002/2016JD025269>

Battan, L. J. (1973). *Radar observations of the atmosphere* (p. 279). University of Chicago Press.

Brook, M., Nakano, M., Krehbiel, P., & Takeuti, T. (1982). The electrical structure of the Hokuriku winter thunderstorms. *Journal of Geophysical Research*, 87, 1207–1215. <https://doi.org/10.1029/jc087ic02p01207>

Bruning, E. C., & MacGorman, D. M. (2013). Theory and observations of controls on lightning flash spectra. *Journal of the Atmospheric Sciences*, 70, 4012–4029. <https://doi.org/10.1175/JAS-D-12-0289.1>

Cober, S. G., Isaac, G. A., Korolev, A. V., & Walter, J. (2001). Assessing cloud-phase conditions. *Journal of Applied Meteorology and Climatology*, 40, 1967–1983. [https://doi.org/10.1175/1520-0450\(2001\)040<1967:ACPC>2.0.CO;2](https://doi.org/10.1175/1520-0450(2001)040<1967:ACPC>2.0.CO;2)

Crowe, C., Market, P., Pettegrew, B., Melick, C., & Podzimek, J. (2006). An investigation of thundersnow and deep snow accumulations. *Geophysical Research Letters*, 33, L24812. <https://doi.org/10.1029/2006GL028214>

Curran, E. B., Holle, R. L., & Lopez, R. E. (2000). Lightning casualties and damages in the United States from 1959–1994. *Journal of Climate*, 13, 3448–3464. [https://doi.org/10.1175/1520-0442\(2000\)013<3448:lccadit>2.0.co;2](https://doi.org/10.1175/1520-0442(2000)013<3448:lccadit>2.0.co;2)

Delene, D., & Poellot, M. (2020). UND Cloud Microphysics IMPACTS. Dataset available online from the NASA Global Hydrology Resource Center DAAC. Huntsville, AL, USA. <https://doi.org/10.5067/IMPACTS/MULTIPLE/DATA101>

Doviak, R. J., Bringi, V., Ryzhkov, A., Zahrai, A., & Zrnić, D. (2000). Considerations for polarimetric upgrades to operational WSR-88D radars. *Journal of Atmospheric and Oceanic Technology*, 17, 257–278. [https://doi.org/10.1175/1520-0426\(2000\)017<0257:CFPUTO>2.0.CO;2](https://doi.org/10.1175/1520-0426(2000)017<0257:CFPUTO>2.0.CO;2)

Dye, J. E., & Bansemer, A. (2019). Electrification in mesoscale updrafts of deep stratiform and anvil clouds in Florida. *Journal of Geophysical Research: Atmospheres*, 124, 1021–1049. <https://doi.org/10.1029/2018JD029130>

Dye, J. E., & Willett, J. C. (2007). Observed enhancement of reflectivity and the electric field in long-lived Florida anvils. *Monthly Weather Review*, 135(10), 3362–3380. <https://doi.org/10.1175/MWR3484.1>

Emory, A. E., McLinden, M., Schreier, M., & Wick, G. A. (2015). An introduction to the NASA East Pacific Origins and Characteristics of Hurricanes (EPOCH) field campaign. *Tropical Cyclone Research and Review*, 4, 124–131. <https://doi.org/10.6057/2015TCRRh3.03>

Giangrande, S. E., Toto, T., Bansemer, A., Kumjian, M. R., Mishra, S., & Ryzhkov, A. V. (2016). Insights into riming and aggregation processes as revealed by aircraft, radar, and disdrometer observations for a 27 April 2011 widespread precipitation event. *Journal of Geophysical Research: Atmospheres*, 121, 5846–5863. <https://doi.org/10.1002/2015JD024537>

Gordon, M., & Taylor, P. A. (2009). The electric field during blowing snow events. *Boundary-Layer Meteorology*, 130, 97–115. <https://doi.org/10.1007/s10546-008-9333-7>

Harkema, S. S., Berndt, E. B., & Schultz, C. J. (2020). Characterization of snowfall rates, totals, and snow-to-liquid ratios in electrified snowfall events identified by the geostationary lightning mapper. *Weather and Forecasting*, 35, 673–689. <https://doi.org/10.1175/WAF-D-19-0126.1>

Harkema, S. S., Schultz, C. J., Berndt, E. B., & Bitzer, P. M. (2019). Geostationary lightning mapper flash characteristics of electrified snowfall events. *Weather and Forecasting*, 34, 1571–1585. <https://doi.org/10.1175/WAF-D-19-0082.1>

Heinselman, P. L., & Ryzhkov, A. V. (2006). Validation of Polarimetric Hail Detection. *Weather and Forecasting*, 21(5), 839–850. <https://doi.org/10.1175/WAF956.1>

Helmus, J. J., & Collis, S. M. (2016). The Python ARM Radar Toolkit (Py-ART), a library for working with weather radar data in the Python programming language. *Journal of Open Research Software*, 4(1), p. e25. <https://doi.org/10.5334/jors.119>

- Hendry, A., & McCormick, G. C. (1976). Radar observations of alignment of precipitation particles by electrostatic fields in thunderstorms. *Journal of Geophysical Research*, *81*, 5353–5357. <https://doi.org/10.1029/jc081i030p05353>
- Heymsfield, A. J., & Kajikawa, M. (1987). An improved approach to calculating terminal velocities of plate-like crystals and graupel. *Journal of the Atmospheric Sciences*, *44*, 1088–1099. [https://doi.org/10.1175/1520-0469\(1987\)044<1088:aiatct>2.0.co;2](https://doi.org/10.1175/1520-0469(1987)044<1088:aiatct>2.0.co;2)
- Heymsfield, A. J., & Miloshevich, L. M. (1988). Evaluation of liquid water measuring instruments in cold clouds sampled during FIRE. *Journal of the Atmospheric Sciences*, *6*, 378–388.
- Heymsfield, A. J., & Westbrook, C. D. (2010). Advances in the estimation of ice particle fall speeds using laboratory and field measurements. *Journal of the Atmospheric Sciences*, *67*, 2469–2482. <https://doi.org/10.1175/2010jas3379.1>
- Heymsfield, G., Bidwell, S., Caylor, I. J., Ameen, S., Nicholson, S., Bonczyk, W., et al. (1996). The EDOP radar system on the high-altitude NASA ER-2 aircraft. *Journal of Atmospheric and Oceanic Technology*, *13*, 795–809. [https://doi.org/10.1175/1520-0426\(1996\)013<0795:TERSOT>2.0.CO;2](https://doi.org/10.1175/1520-0426(1996)013<0795:TERSOT>2.0.CO;2)
- Heymsfield, G. M., Li, L., & McLinden, M. L. (2020). ER-2 X-band Radar (EXRAD) IMPACTS. Dataset available online from the NASA Global Hydrology Resource Center DAAC, Huntsville, AL, USA. <https://10.5067/IMPACTS/EXRAD/DATA101>
- Hobbs, B., Sorenson, C., Stith, E., Bennett, R., & Hoffmann, G. (2020). NASA ER-2 Navigation Data IMPACTS. Dataset available online from the NASA Global Hydrology Resource Center DAAC, Huntsville, AL, USA. <https://10.5067/IMPACTS/ER2/DATA101>
- Holle, R. L., Lopez, R. E., Howard, K. W., Cummins, K. L., Malone, M. D., & Krider, E. P. (1997). An isolated winter cloud-to-ground lightning flash causing damage and injury in Connecticut. *Bulletin of the American Meteorological Society*, *78*, 437–441. [https://doi.org/10.1175/1520-0477\(1997\)078<0437:aiwctg>2.0.co;2](https://doi.org/10.1175/1520-0477(1997)078<0437:aiwctg>2.0.co;2)
- Holle, R. L., Lopez, R. E., & Zimmermann, C. (1999). Updated recommendations for lightning safety-1998. *Bulletin of the American Meteorological Society*, *80*, 2035–2041. [https://doi.org/10.1175/1520-0477\(1999\)080<2035:urfls>2.0.co;2](https://doi.org/10.1175/1520-0477(1999)080<2035:urfls>2.0.co;2)
- Hubbert, J. C., Ellis, S. M., Chang, W., Rutledge, S., & Dixon, M. (2014). Modeling and interpretation of s-band ice crystal depolarization signatures from data obtained by simultaneously transmitting horizontally and vertically polarized fields. *Journal of Applied Meteorology and Climatology*, *53*, 1659–1677. <https://doi.org/10.1175/JAMC-D-13-0158.1>
- Hubbert, J. C., Ellis, S. M., Dixon, M., & Meymaris, G. (2010). Modeling, error analysis, and evaluation of dual-polarization variables obtained from simultaneous horizontal and vertical polarization transmit radar. Part I: Modeling and antenna errors. *Journal of Atmospheric and Oceanic Technology*, *27*, 1583–1598. <https://doi.org/10.1175/2010jtecha1336.1>
- Kennedy, P. C., & Rutledge, S. A. (2011). S-band dual-polarization radar observations of winter storms. *Journal of Applied Meteorology and Climatology*, *50*, 844–858. <https://doi.org/10.1175/2010JAMC2558.1>
- Kitagawa, N., & Michimoto, K. (1994). Meteorological and electrical aspects of winter thunderclouds. *Journal of Geophysical Research*, *99*, 10713–10721. <https://doi.org/10.1029/94jd00288>
- Krehbiel, P. R., Chen, T., McCrary, S., Rison, W., Gray, G., & Brook, M. (1996). The use of dual-channel circular-polarization radar observations for remotely sensing storm electrification. *Meteorology and Atmospheric Physics*, *59*, 65–82. <https://doi.org/10.1007/bf01032001>
- Kumjian, M. R. (2013). Principles and applications of dual-polarization weather radar. Part III: Artifacts. *Journal of Operational Meteorology*, *1*(21), 265–274. <https://doi.org/10.15191/nwajom.2013.0121>
- Kumjian, M. R., & Deierling, W. (2015). Analysis of thundersnow storms over Northern Colorado. *Weather and Forecasting*, *30*, 1469–1490. <https://doi.org/10.1175/waf-d-15-0007.1>
- Kumjian, M. R., Mishra, S., Giangrande, S. E., Toto, T., Ryzhkov, A. V., & Bansemer, A. (2016). Polarimetric radar and aircraft observations of saggy bright bands during MC3E. *Journal of Geophysical Research: Atmospheres*, *121*, 3584–3607. <https://doi.org/10.1002/2015JD024446>
- Lance, S., Brook, C. A., Rogers, D., & Gordon, J. A. (2010). Water droplet calibration of the Cloud Droplet Probe (CDP) and in-flight performance in liquid, ice, and mixed phase clouds during ARCPAC. *Atmospheric Measurement Techniques*, *3*, 1683–1706. <https://doi.org/10.5194/amt-3-1683-2010>
- Lawson, R. P., O'Connor, D., Zmarzly, P., Weaver, K., Baker, B., Mo, Q., & Jonsson, H. (2006). The 2D-S (Stereo) Probe: Design and preliminary tests of a new airborne, high-speed, high-resolution particle imaging probe. *Journal of Atmospheric and Oceanic Technology*, *23*, 1462–1477. <https://doi.org/10.1175/JTECH1927.1>
- Liu, H., & Chandrasekar, V. (2000). Classification of hydrometeors based on polarimetric radar measurements: Development of fuzzy logic and neuro-fuzzy systems, and in situ verification. *Journal of Atmospheric and Oceanic Technology*, *17*, 140–164. [https://doi.org/10.1175/1520-0426\(2000\)017<0140:COHBOP>2.0.CO;2](https://doi.org/10.1175/1520-0426(2000)017<0140:COHBOP>2.0.CO;2)
- Locatelli, J. D., & Hobbs, P. V. (1974). Fall speeds and masses of solid precipitation particles. *Journal of Geophysical Research*, *79*(15), 2185–2197. <https://doi.org/10.1029/JC079i015p02185>
- Mach, D. M., Bateman, M. G., & Schultz, C. J. (2020). Lightning Instrument Package (LIP) IMPACTS. Dataset available online from the NASA Global Hydrology Resource Center DAAC, Huntsville, AL, USA. <https://10.5067/IMPACTS/LIP/DATA101>
- Mach, D. M., Blakeslee, R. J., Bailey, J. C., Farrell, W. M., Goldberg, R. A., Desch, M. D., & Houser, J. G. (2005). Lightning optical pulse statistics from storm overflights during the Altus Cumulus Electrification Study. *Atmospheric Research*, *76*, 386–401. <https://doi.org/10.1016/j.atmosres.2004.11.039>
- Mach, D. M., Blakeslee, R. J., & Bateman, M. G. (2011). Global electric circuit implications of combined aircraft storm electric current measurements and satellite-based diurnal lightning statistics. *Journal of Geophysical Research*, *116*. <https://doi.org/10.1029/2010JD014462>
- Mach, D. M., Blakeslee, R. J., Bateman, M. G., & Bailey, J. C. (2009). Electric fields, conductivity, and estimated currents from aircraft overflights of electrified clouds. *Journal of Geophysical Research*, *114*, D10204. <https://doi.org/10.1029/2008JD011495>
- Mach, D. M., Blakeslee, R. J., Bateman, M. G., & Bailey, J. C. (2010). Comparisons of total currents based on storm location, polarity, and flash rates derived from high-altitude aircraft overflights. *Journal of Geophysical Research*, *115*, D03201. <https://doi.org/10.1029/2009JD012240>
- Mach, D. M., & Koshak, W. J. (2007). General matrix inversion technique for the calibration of electric field sensor arrays on aircraft platforms. *Journal of Atmospheric and Oceanic Technology*, *24*, 1576–1587. <https://doi.org/10.1175/JTECH2080.1>
- Market, P. S., & Becker, A. E. (2009). A study of lightning flashes attending periods of banded snowfall. *Geophysical Research Letters*, *36*, L01809. <https://doi.org/10.1029/2008GL036317>
- Market, P. S., Oravetz, A. M., Gaede, D., Bookbinder, E., Lupo, A. R., Melick, C. J., et al. (2006). Proximity Soundings of thundersnow in the Central United States. *Journal of Geophysical Research*, *111*, D19208. <https://doi.org/10.1029/2006JD007061>
- McMurdie, L. A., Heymsfield, G., Yorks, J. E., & Braun, S. A. (2019). Investigation of Microphysics and Precipitation for Atlantic Coast-Threatening Snowstorms (IMPACTS) Collection [indicate subset used]. Data available online [ <http://ghrc.nsstc.nasa.gov/>] from the NASA EOSDIS Global Hydrology Resource Center Distributed Active Archive Center, Huntsville, AL, USA. <https://doi.org/10.5067/IMPACTS/DATA101>

- McMurdie, L. A., Heymsfield, G. M., Braun, S. A., Yorks, J. E., Finlon, J., & McDonald, V. (2020). *Investigation of microphysics and precipitation for atlantic-coast threatening Snowstorms (IMPACTS): Preliminary results from the first deployment in winter 2020*. AGU Fall Meeting, 2020.
- Molthan, A. M., & Petersen, W. A. (2011). Incorporating ice crystal scattering databases in the simulation of millimeter-wavelength radar reflectivity. *Journal of Atmospheric and Oceanic Technology*, *28*, 337–351. <https://doi.org/10.1175/2010jtecha1511.1>
- Nelson, J. T., & Baker, M. B. (2003). Charging of ice-vapor interfaces: Applications to thunderstorms. *Atmospheric Chemistry and Physics*, *3*, 1237–1252. <https://doi.org/10.5194/acp-3-1237-2003>
- Rauber, R., Wegman, J., Plummer, D. M., Rosenow, A. A., Peterson, M. L., Mcfarquhar, G., et al. (2014). Stability and charging characteristics of the comma head region of continental winter cyclones. *Journal of the Atmospheric Sciences*, *71*, 1559–1582. <https://doi.org/10.1175/JAS-D-13-0253.1>
- Rauber, R. M., Janiszewski, A., Zaremba, T., & Varcie, M. (2020). Mobile UIUC soundings IMPACTS. Dataset available online from the NASA global Hydrology Resource center DAAC. Huntsville, AL, USA. <https://doi.org/10.5067/IMPACTS/SOUNDING/DATA101>
- Reimel, K. J., & Kumjian, M. R. (2020). Evaluation of KDP estimation algorithm performance in rain using a known-truth framework. *Journal of Atmospheric and Oceanic Technology*. <https://doi.org/10.1175/JTECH-D-20-0060.1>
- Rust, W. D., & Trapp, R. J. (2002). Initial balloon soundings of the electric field in winter nimbostratus clouds in the USA. *Geophysical Research Letters*, *29*, 20–21. <https://doi.org/10.1029/2002GL015278>
- Ryzhkov, A., & Zrnić, D. S. (2007). Depolarization in ice crystals and its effect on radar polarimetric measurements. *Journal of Atmospheric and Oceanic Technology*, *24*, 1256–1267. <https://doi.org/10.1175/jtech2034.1>
- Ryzhkov, A. V. (2007). The impact of beam broadening on the quality of radar polarimetric data. *Journal of Atmospheric and Oceanic Technology*, *24*, 729–744. <https://doi.org/10.1175/jtech2003.1>
- Saunders, C. P. R., Bax-Norman, H., Emersic, C., Avila, E. E., & Castellano, N. E. (2006). Laboratory studies of the effect of cloud conditions on graupel/crystal charge transfer in thunderstorm electrification. *Quarterly Journal of the Royal Meteorological Society*, *132*, 2653–2673. <https://doi.org/10.1256/qj.05.218>
- Schultz, C. J., Allen, R. E., Murphy, K. M., Herzog, B. S., Weiss, S. A., & Ringhausen, J. S. (2021). Investigation of cloud-to-ground flashes in the non-precipitation stratiform region of a mesoscale convective system on 20 August 2019 and implications for decision support services. *Weather and Forecasting*, *36*, 717–735. <https://doi.org/10.1175/WAF-D-20-0095.1>
- Schultz, C. J., Lang, T. J., Bruning, E. C., Calhoun, K. M., Harkema, S., & Curtis, N. (2018). Characteristics of lightning within electrified snowfall events using lightning mapping arrays. *Journal of Geophysical Research*, *123*, 2347–2367. <https://doi.org/10.1002/2017JD027821>
- Schuur, T. J., & Rutledge, S. A. (2000). Electrification of stratiform regions in mesoscale convective systems. Part 1: An observational comparison of symmetric and asymmetric MCSs. *Journal of the Atmospheric Sciences*, *57*, 1961–1982. [https://doi.org/10.1175/1520-0469\(2000\)057<1961:EOSRIM>2.0.CO;2](https://doi.org/10.1175/1520-0469(2000)057<1961:EOSRIM>2.0.CO;2)
- Scott, R. D., Krehbiel, P. R., & Rison, W. (2001). The use of simultaneous horizontal and vertical transmissions for dual-polarization radar meteorological observations. *Journal of Atmospheric and Oceanic Technology*, *18*, 629–648. [https://doi.org/10.1175/1520-0426\(2001\)018<0629:tuosha>2.0.co;2](https://doi.org/10.1175/1520-0426(2001)018<0629:tuosha>2.0.co;2)
- Seliga, T. A., & Bringi, V. N. (1976). Potential use of radar differential reflectivity measurements at orthogonal polarizations for measuring precipitation. *Journal of Applied Meteorology*, *15*, 69–76. [https://doi.org/10.1175/1520-0450\(1976\)015<0069:puordr>2.0.co;2](https://doi.org/10.1175/1520-0450(1976)015<0069:puordr>2.0.co;2)
- Spencer, R., Hood, R., LaFontaine, F., Smith, E. A., Platt, R., Galliano, J., et al. (1994). High-resolution imaging of rain systems with the advanced microwave precipitation radiometer. *Journal of Atmospheric and Oceanic Technology*, *11*, 849–857. [https://doi.org/10.1175/1520-0426\(1994\)011<0849:HRIORS>2.0.CO;2](https://doi.org/10.1175/1520-0426(1994)011<0849:HRIORS>2.0.CO;2)
- Stano, G. T., Smith, M. R., & Schultz, C. J. (2019). Development and evaluation of the GLM stoplight product for lightning safety. *Journal of Operational Meteorology*, *7*(7), 92–104. <https://doi.org/10.15191/nwajom.2019.0707>
- Straka, J. M., Zrnić, D. S., & Ryzhkov, A. V. (2000). Bulk hydrometeor classification and quantification using polarimetric radar data: Synthesis of relations. *Journal of Applied Meteorology*, *39*, 1341–1372. [https://doi.org/10.1175/1520-0450\(2000\)039<1341:bhcaqu>2.0.co;2](https://doi.org/10.1175/1520-0450(2000)039<1341:bhcaqu>2.0.co;2)
- Takahashi, T. (1978). Riming electrification as a charge generation mechanism in thunderstorms. *Journal of the Atmospheric Sciences*, *35*, 1536–1548. [https://doi.org/10.1175/1520-0469\(1978\)035<1536:reaacg>2.0.co;2](https://doi.org/10.1175/1520-0469(1978)035<1536:reaacg>2.0.co;2)
- Takeuti, T., Nakano, M., Brook, M., Raymond, D. J., & Krehbiel, P. (1978). The anomalous winter thunderstorms of the Hokuriku coast. *Journal of Geophysical Research*, *83*, 2385–2394. <https://doi.org/10.1029/jc083ic05p02385>
- Thompson, E. J., Rutledge, S. A., Dolan, B., Chandrasekar, V., & Cheong, B. L. (2014). A dual-polarization radar hydrometeor classification algorithm for winter precipitation. *Journal of Atmospheric and Oceanic Technology*, *31*, 1457–1481. <https://doi.org/10.1175/JTECH-D-13-00119.1>
- Tsenova, B., Barakova, D., & Mitzeva, R. (2017). Numerical study on the effect of charge separation at low cloud temperature and effective water content on thunderstorm electrification. *Atmospheric Research*, *184*, 1–14. <https://doi.org/10.1016/j.atmosres.2016.09.011>
- Unidata (2021). Integrated data viewer. <https://doi.org/10.5065/D6H70CW6>
- Vivekanandan, J., Zrnić, D. S., Ellis, S. M., Oye, R., Ryzhkov, A. V., & Straka, J. (1999). Cloud microphysics retrieval using S-band dual-polarization radar measurements. *Bulletin of the American Meteorological Society*, *80*, 381–388. [https://doi.org/10.1175/1520-0477\(1999\)080<0381:CMRUSB>2.0.CO;2](https://doi.org/10.1175/1520-0477(1999)080<0381:CMRUSB>2.0.CO;2)
- Wang, Y., & Chandrasekar, V. (2006). Polarization isolation requirements for linear dual-polarization weather radar in simultaneous transmission mode of operation. *IEEE Transactions on Geoscience and Remote Sensing*, *44*, 2019–2028. <https://doi.org/10.1109/TGRS.2006.872138>
- Yair, Y., Reuveni, Y., Katz, S., Price, C., & Yaniv, R. (2019). Strong electric fields observed during snow storms on Mt. Hermon, Israel. *Atmospheric Research*, *215*, 208–213. <https://doi.org/10.1016/j.atmosres.2018.09.009>
- Yang-Martin, M., & Bennett, J. R. (2020). P-3 Meteorological and Navigation Data IMPACTS. Dataset available online from the NASA ESDIS Global Hydrology Resource Center Distributed Active Archive Center. Huntsville, AL, USA. <https://doi.org/10.5067/IMPACTS/P3/DATA101>